The genetic driver of Acute Necrotizing Encephalopathy, *RANBP2*, regulates the inflammatory response to Influenza A virus infection

Sophie Desgraupes[1], Benoît Gouy[1], Suzon Perrin[1], Adrien Decorsière[1], Yifan E Wang[2], Alexander F. Palazzo[2], Sandie Munier[3], Nathalie J. Arhel[1*]

[1] Institut de Recherche en Infectiologie, University of Montpellier, CNRS UMR9004, 1919 route de Mende, 34090 Montpellier, France

[2] Department of Biochemistry, University of Toronto, 661 University Avenue, Toronto, ON M5G 1M1, Canada

[3] Institut Pasteur, Université Paris Cité, Unité Lyssavirus, Epidémiologie et Neuropathologie, F-75015, Paris, France

* Correspondence: nathalie.arhel@cnrs.fr

ABSTRACT

Influenza virus infections can cause severe complications such as Acute Necrotizing Encephalopathy (ANE), which is characterised by rapid onset pathological inflammation following febrile infection. Heterozygous dominant mutations in the nucleoporin RANBP2/Nup358 predispose to influenza-triggered ANE1. The aim of our study was to determine whether RANBP2 plays a role in IAV-triggered inflammatory responses. We found that the depletion of RANBP2 in a human airway epithelial cell line increased IAV genomic replication by favouring the import of the viral polymerase subunits, PB1, PB2 and PA, and promoted an abnormal accumulation of some viral segments in the cytoplasm. In human primary macrophages, this corroborated with an enhanced production of the pro-inflammatory chemokines CXCL8, CXCL10, CCL2, CCL3 and CCL4. Then, using CRISPR-Cas9 knock-in for the ANE1 disease variant RANBP2-T585M, we demonstrated that the point mutation is sufficient to drive CXCL10 expression following activation downstream of RIG-I and leads to a redistribution of RANBP2 away from the nuclear pore. Together, our results reveal that RANBP2 regulates influenza RNA replication and nuclear export, triggering hyper-inflammation, offering insight into ANE pathogenesis.

INTRODUCTION

Influenza viral infections are responsible for seasonal epidemics with respiratory manifestations but can also lead to severe complications. Among these, Acute Necrotizing Encephalopathy (ANE), also called ANE of Childhood (ANEC), is a severe reaction to febrile infection that is characterized by rapid progression and very poor prognosis (Lee et al., 2023; Sakuma et al., 2025; Wu et al., 2015; Mizuguchi et al., 2007). Influenza viruses are thought to be responsible for ~50% of all ANE episodes and are associated with high morbidity and mortality (Bartolini et al., 2024; Jiang et al., 2022; Mizuguchi et al., 2007; Neilson et al., 2003; Chatur et al., 2022; Bashiri et al., 2020). Although the pathogenesis is unclear, a hyperinflammatory response triggered by the virus is proposed as the underlying mechanism (Levine et al., 2020; Mizuguchi et al., 2007; Sugaya, 2002), and early anti-inflammatory therapy may help mitigate the disease (Chatur et al., 2022; Koh et al., 2019; Okumura et al., 2009).

Influenza viruses belong to the *Orthomyxoviridae* family and are classified into types, Influenza A and B being the most prevalent ones associated with seasonal flu cases. Influenza A is further divided into subtypes based on their surface glycoproteins, haemagglutinin (HA) and neuraminidase (NA). The H1N1 and H3N2 strains are responsible for major outbreaks and epidemics, and in the 2024-2025 winter season,

there has been an unprecedented surge in H1N1 cases, leading to an unusual spike in hospitalizations and ANE in children (Bartolini et al., 2024).

The Influenza A virus (IAV) is an enveloped particle containing 8 negative-sense single-stranded viral RNA (vRNA) gene segments, each packaged by nucleoprotein (NP) into a viral ribonucleoprotein (vRNP) complex, and associated with the viral polymerase complex (PB1, PB2, and PA). Unlike most RNA viruses, IAV replicates in the nucleus and hijacks the nuclear pore complex (NPC) machinery for four critical steps of its replication cycle. (i) After endocytosis and uncoating, vRNPs are trafficked to the nucleus where the viral polymerase transcribes the viral genome. (ii) Capped and polyadenylated mRNAs are exported into the cytoplasm for translation by cytoplasmic ribosomes. (iii) The newly translated viral proteins, including NP, PB1, PB2 and PA, are imported back into the nucleus, which allows the viral polymerase to replicate the viral genome into complementary RNAs (cRNA) and genomic vRNA. (iv) Lastly, new vRNPs, assembled with M1 and NS2/NEP, are exported back from the nucleus for incorporation into budding virions (Dou et al., 2018; Carter and Iqbal, 2024; Fodor and Te Velthuis, 2020; Zhu et al., 2023).

Many viral and host factors are thought to contribute to severe influenza, and genetic susceptibility particularly in genes that regulate innate signalling and antiviral response, has been reported (Mettelman and Thomas, 2021; Clohisey and Baillie, 2019; Gounder and Boon, 2019). However, the mechanisms that drive severe influenza-triggered ANE in previously healthy children are not known. One clue to understanding the pathogenesis of influenza-associated ANE comes from genetic susceptibility in familial, recurrent cases, known as ANE1 (or ADANE) (Neilson et al., 2003). Patients with ANE1 present with autosomal dominant missense mutations in *RANBP2* and have a significantly increased lifetime risk of developing ANE (Neilson et al., 2009). Mutations in *RANBP2* increase the risk of relapse and recurrence (Levine et al., 2020; Chatur et al., 2022) and may associate with greater morbidity and mortality.

RANBP2 (Nup358) is a cytoplasmic fibril (CF) nucleoporin that regulates nucleocytoplasmic transport by interacting with nuclear transport receptors such as Karyopherin α/β and CRM1/Exportin 1 (Yokoyama et al., 1995; Hutten et al., 2008). Additional functions have been attributed to RANBP2 at the NPC, many of which are linked to its C-terminal domain (CTD) E3 SUMO ligase activity, and away from the NPC, namely at annulate lamellae, mitochondria-endoplasmic reticulum junctions and in the nucleus (Desgraupes et al., 2023). Moreover, at least 4 protein isoforms have been identified for RANBP2, however, it is not known if these have distinct functions or subcellular localisations. The predominant ANE1-associated mutation (c.C1754T, p.T585M), and most other pathogenic mutations in RANBP2, all cluster in the N-terminal domain (NTD), which is responsible for anchoring to NPCs (Jiang et al., 2022; Joseph and Dasso, 2008). This suggests that the localization of RANBP2 to CF may be physiologically essential, although no changes in localisation could be demonstrated following the overexpression of disease variants (Shen et al., 2021; Bley et al., 2022).

Previous work showed that RANBP2 can modulate viral infection of several viruses, such as Adenovirus (Carlon-Andres et al., 2020), Herpes simplex virus type 1 (HSV-1) (Copeland et al., 2009; Hofemeister and O'Hare, 2008) and Human immunodeficiency virus type 1 (HIV-1) (Bichel et al., 2013; Di Nunzio et al., 2012; Schaller et al., 2011; Zhang et al., 2010)**,** however no work has uncovered a role for RANBP2 in Influenza virus infection. In fact, although some studies showed that NPC components can impact the replication and transcription of Influenza virus, such as Nup62, Nup98 and Nup153, RANBP2 was not identified as a host factor for Influenza virus (Khanna et al., 2024; Watanabe et al., 2010; Munier et al., 2013).

Previous work also showed that RANBP2 can modulate innate immune signalling, however this activity was consistently attributed to its E3 SUMO ligase activity or Cyclophilin-homology motif in the CTD (Maarifi et al., 2018; Portilho et al., 2016; Shen et al., 2021; Li et al., 2023), and no work has yet demonstrated a role for the NTD where ANE1 mutations are clustered.

88 The aim of our study was to determine how RANBP2 contributes to or regulates inflammatory responses
89 to infection by Influenza virus. We show that RANBP2 impacts the replication of genomic vRNAs of IAV
90 into cRNA by controlling the re-import of newly translated viral polymerase complex. Interestingly,
91 RANBP2 also controls RNP export from the nucleus but in a segment-specific manner, only impacting the
92 long segments encoding the PB1, PB2 and PA proteins, thus leading to their cytoplasmic accumulation and
93 triggering hyper-inflammation, which could provide a first clue in understanding the pathogenesis of ANE.

94 **RESULTS**

95 **Knockdown of RANBP2 stimulates non-productive Influenza vRNA replication in infected cells**

96 To investigate the role of RANBP2 in IAV infection, RANBP2-knockdown (RANBP2-KD) was induced in A549
97 human alveolar cells by lentiviral vector (LV) transduction before infection with A/WSN/1933(H1N1) virus
98 at MOI 0.5. Supernatants were harvested at 10 h post-infection (hpi) to investigate the production of
99 infectious viral particles by TCID50 titration. No differences were observed between the Control and
100 RANBP2-KD cells, suggesting that RANBP2 had no effect on the production of infectious particles **(Figure**
101 **1A, Figure S1)**.

102 However, an unexpected phenotype was observed for viral RNA quantification in both A549 and the
103 monocytic cell line THP-1. Infection kinetics were performed and viral RNA levels were determined at early
104 (2 h) and late (6, 8, 16 and 24 h) time points using qPCR primers recognizing M1 on segment 7. In the
105 monocytic cell line THP-1 **(Figure 1B)** and in A549 cells **(Figure 1C)**, a significant increase of M1 RNA was
106 induced in RANBP2-KD cells. Although the change was most striking in THP-1 cells (40-fold), this led to
107 considerable cell death and, therefore, A549 cells were preferred for further analysis. The increase in viral
108 RNA was confirmed with another IAV segment, encoding the NP **(Figure 1D)**, and appeared to be specific
109 since no increase was observed for any of the housekeeping genes that were measured **(Figure 1E)**.
110 Together, these data suggested that RANBP2 is involved in controlling Influenza viral RNA synthesis but
111 that this does not translate into increased productive infection.

112 Because different types of viral RNAs are produced during the IAV life cycle, we investigated which RNAs
113 are impacted by the depletion of RANBP2. Tagged RT primers were used to specifically recognize the
114 negative-sense genomic vRNA sequence or the positive-sense cRNA sequence in order to specifically
115 reverse transcribe (RT) each type of viral RNA **(Figure S2A)**. First, the specificity of each primer was
116 validated by amplifying only vRNAs after vRNA-specific RT, or only cRNAs after cRNA-specific RT, while not
117 amplifying any target in non-infected cells **(Figure S2B)**. In RANBP2-KD cells, we observed a significant
118 increase of both vRNAs and cRNAs **(Figure 1F)**, thus showing that RANBP2 is involved in IAV RNA
119 replication. Although this was unexpected given the absence of phenotype in terms of viral production,
120 the marked increase in cRNA and vRNA levels suggested an enhancement in viral genome replication.

121 Having observed an increase in genomic vRNAs, we tested if this correlated with more newly produced
122 vRNPs. As previously, A549 cells were transduced with Control- or RANBP2-shRNAs then infected with IAV
123 (MOI 0.5). At 8 hpi, the distribution of NP was investigated by immunofluorescence. Although export is
124 ongoing in every condition, RANBP2-KD cells showed a striking increase in cytoplasmic NP **(Figure 1G and**
125 **1H, Figure S3).** In order to determine if signal corresponded to vRNPs or free NP in the cytoplasm, we
126 performed co-stainings with other components of vRNPs (i.e. PB1 and PA). We observed a co-localisation
127 of cytoplasmic NP with PB1 and with PA **(Figure 1I and 1J, Figure S4)**, showing that RANBP2-KD induces an
128 increase in vRNPs exported to the cytoplasm.

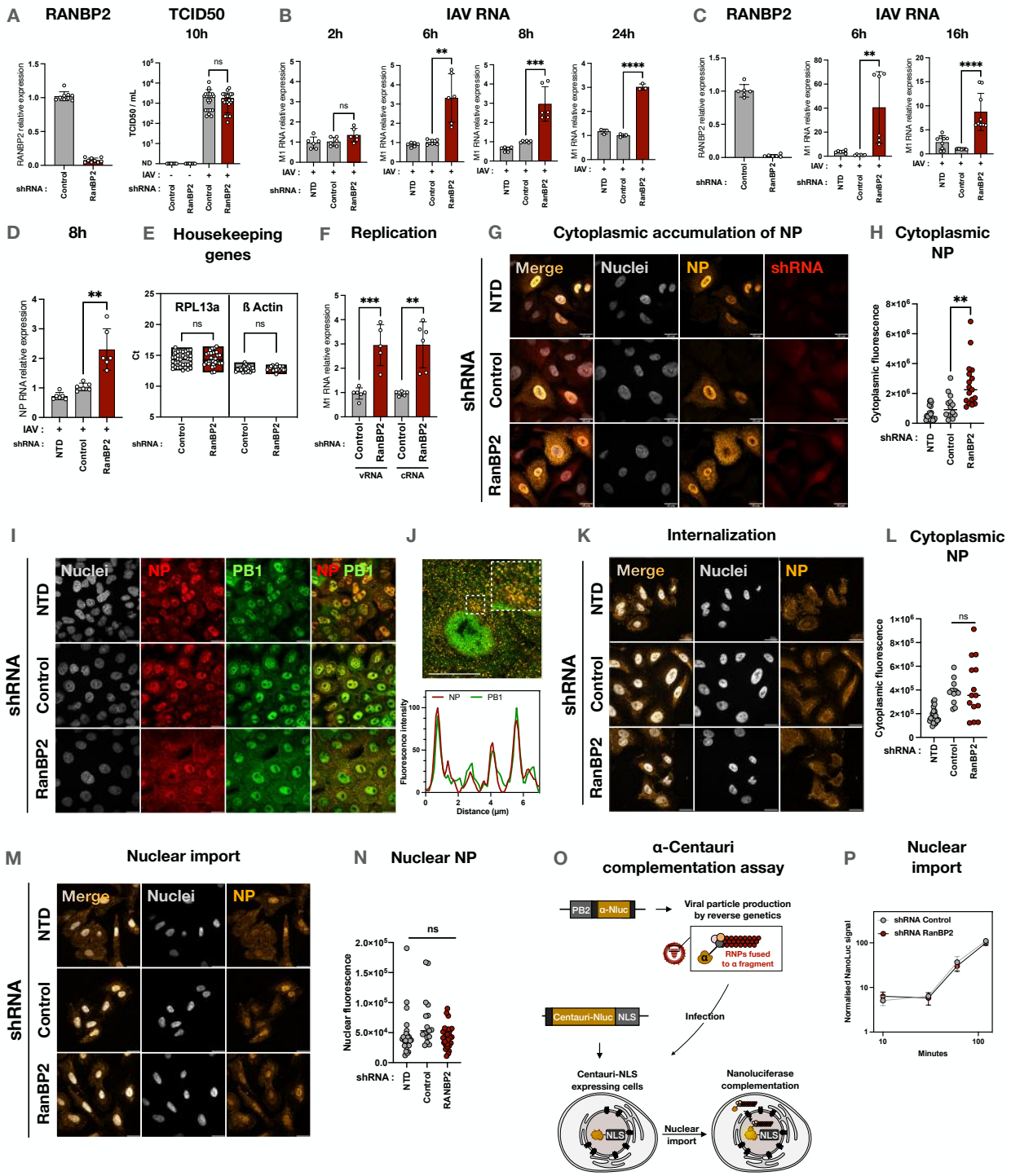

Figure 1: Knockdown of RANBP2 stimulates non-productive Influenza vRNA replication in infected cells without altering the initial vRNP import into the nucleus. (A) A549 cells were transduced with LV shRNA-Control or shRANBP2, and infected with influenza A virus (IAV) (A/WSN/1933) at MOI 0.5. RANBP2 transcripts were quantified by RT-qPCR and normalized on RPL13a housekeeping gene and on the control condition. Supernatants were harvested at 10h post-infection and viral titers were determined by TCID50 assay on MDCK cells. Results represent mean values +/- SD. **(B)** A549 cells or **(C)** THP-1 cells were transduced with LV shRNA-Control or -RANBP2 or not transduced (NTD) then infected with influenza A virus (A/WSN/1933) at MOI 0.5. At the indicated time points, cells were lysed and total intracellular RNAs were extracted. Viral RNAs encoding the Matrix 1 (M1) protein were amplified by RTqPCR. **(D)** Nucleoprotein-encoding (NP) viral RNAs were amplified by RTqPCR in the A549

infected cells. Results from B-C-D are normalized on a housekeeping gene and on the control condition. Results are presented as mean +/- SD. **(E)** Housekeeping gene expression was not affected by the knock down. **(F)** Transduced A549 cells were infected at MOI 0.5 and total intracellular RNAs were extracted at 6h post-infection. Strand-specific reverse transcription (RT) was performed with tagged-primers to amplify separately the genomic viral RNA (vRNA) and the complementary viral RNA (cRNA). M1-encoding viral RNAs were amplified by RTqPCR. Results are normalized on the control condition and presented as mean +/- SD. **(G)** Transduced A549 cells were infected at MOI 0.5 and stained for the NP at 8h post-infection. Scale bar: 20µm. **(H)** Cytoplasmic fluorescence was quantified using the Fiji software. Each dot represents the cytoplasmic fluorescence of a cell, normalized by its area. **(I)** Transduced A549 cells were infected at MOI 0.5 and co-stained for the NP and PB1 proteins at 8h post-infection. Scale bar: 20µm. B**J)** Colocalization was quantified using the Fiji software. **(K)** Transduced A549 cells were infected at MOI 4 and stained for the NP at 1h post-infection. Scale bar: 20µm. **(L)** Confocal Airyscan image processing and quantifications were performed in the Fiji software. Each dot represents the cytoplasmic fluorescence of a cell, normalized by its area. **(M)** Transduced A549 cells were infected at MOI 4 and stained for the NP at 2h post-infection. Scale bar: 20µm. **(N)** Nuclear fluorescence was quantified using the Fiji software. Each dot represents the nuclear fluorescence of a cell. **(O)** Experimental strategy of the Alpha-Centauri assay. IAV (A/WSN/1933) particles containing the PB2 protein fused to a fragment of the NanoLuc (α-Nluc) were produced by reverse genetics. A plasmid containing a nuclear localization signal (NLS) fused to the other fragment of the NanoLuc (Centauri-Nluc) was generated and transfected into A549 cells. Transfected cells were infected at MOI 4 and the luminescence was measured to assess the NanoLuc complementation upon nuclear import of the viral ribonucleoproteins. **(P)** NanoLuc complementation results are normalized on the last time point. Two-tailed unpaired Student's t test. *P < 0.05, **P < 0.002, ***P < 0.0002, ****P < 0.0001, ns: non-significant.

Increased IAV replication does not result from enhanced viral entry into cells or into the nucleus

To determine how vRNA is increased in RANBP2-depleted cells, we first tested whether RANBP2 regulates IAV infection by modulating viral entry into cells and/or nuclei, thereby increasing the quantity of IAV RNA to be copied.

To assess whether RANBP2 regulates cell or nuclear entry, Control or RANBP2-KD cells were infected with IAV (A/WSN/33) at MOI 4 in order to increase signal detection during early steps of the viral cycle, and NP localization was studied by immunofluorescence at 1 hpi to assess internalization, and at 2 h to monitor NP nuclear entry. Results indicate that depletion of RANBP2 from A549 cells affects neither internalization **(Figure 1K and 1L)** nor nuclear import **(Figure 1M and 1N)**.

To further validate these findings, we adapted an Alpha-Centauri protein-complementation assay previously developed to monitor the nuclear import of HIV-1 (Fernandez et al., 2021). Briefly, the NanoLuc protein was expressed as two unequal non-luminescent fragments. The smaller fragment was fused to PB2 (called Alpha), while the larger fragment (Centauri) was fused to a NLS and expressed in A549 cells by lentiviral vector (LV) transduction **(Figure 1O, Figure S5A and S5B)**. Upon vRNP nuclear import, the two fragments reconstitute a functional NanoLuc, generating a measurable signal upon addition of substrate **(Figure S5C)**. No significant differences in luminescence were detected between control and RANBP2-KD cells at 1 and 2 hpi, confirming that RANBP2 is not essential for vRNP nuclear import **(Figure 1P, Figure S5D)**, thus demonstrating that RANBP2 does not regulate IAV vRNP nuclear import.

RANBP2 Knockdown facilitates the nuclear import of the neo-synthesised viral polymerase complex proteins PB1, PB2 and PA

Since RANBP2 does not impact the quantity of template available for replication, we investigated whether it modulates the quantity or transport of the polymerase complex subunits. First, the total levels of PB1, PB2, PA and NP were assessed by Western-Blot at 8 hpi, however, no differences were observed between RANBP2-KD cells and Control cells **(Figure 2A)**, suggesting that RANBP2 does not impact the translation of the viral polymerase complex.

Being an NPC component, we hypothesised that RANBP2 may control the replication of vRNA by regulating the import of the viral polymerase. Therefore, we tested the impact of RANBP2 on the nuclear import of newly synthesised PB1, PB2, and PA subunits. To focus specifically on import, we inhibited vRNP export using a pharmacological inhibitor of CRM1, KPT-330/Selinexor. First, we confirmed that KPT-330 inhibits vRNP export in a dose-dependent manner **(Figure S6A)**, with negligible toxicity **(Figure S6B)** and that

187 inhibition operates from 5 hpi onwards **(Figure S6C)**. Then we performed subcellular fractionation
188 followed by Western blotting at 6 hpi to determine the localisation of the different polymerase subunits.
189 Results revealed an increase in PB1, PB2 and PA protein levels in the nucleus, confirmed by the
190 immunofluorescence detection of nuclear PB1, indicating that the import of the neo-synthesised
191 polymerase is facilitated in the absence of RANBP2 **(Figure 2B and 2C, Figure S7)**.

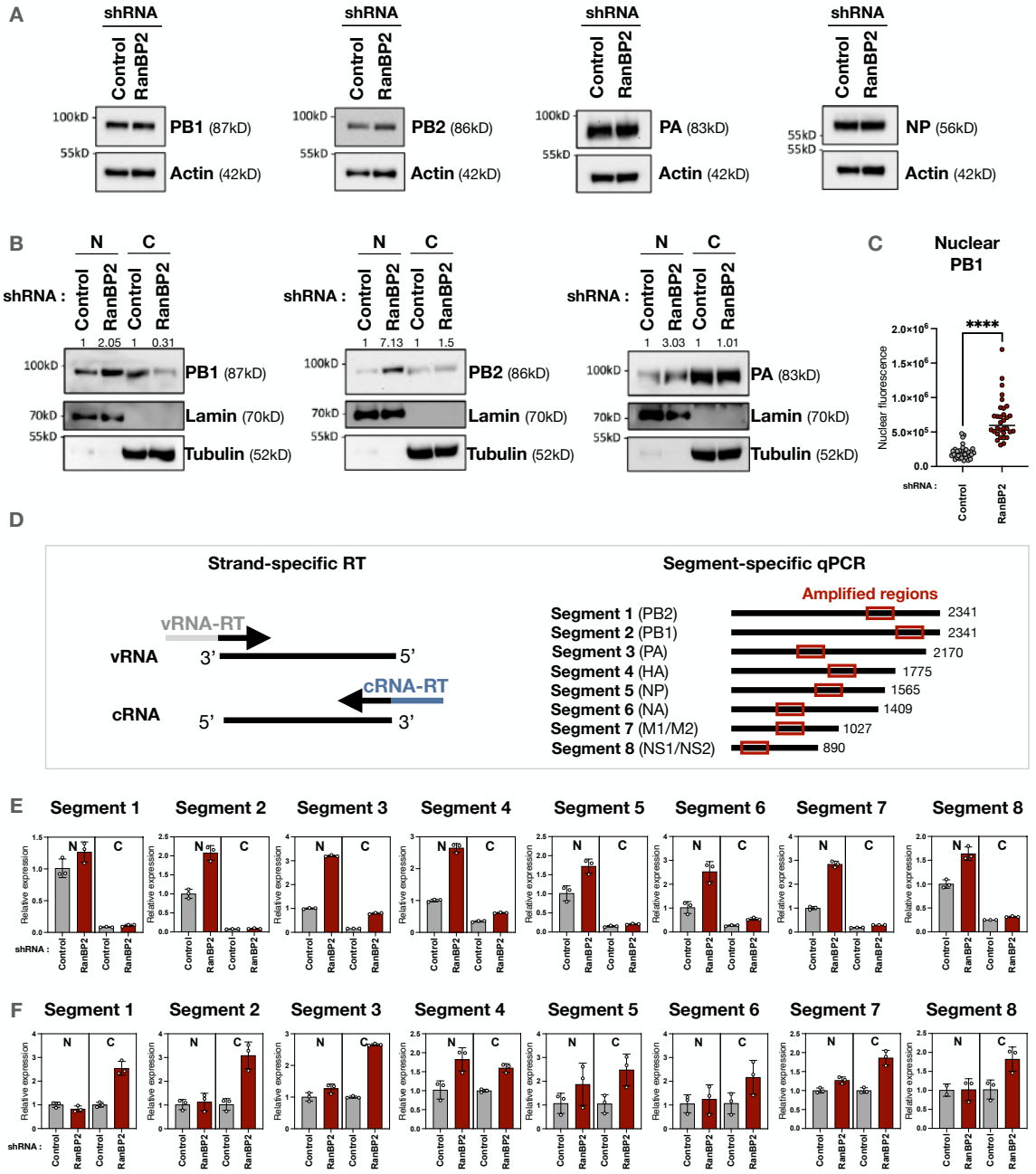

192
193 **Figure 2: RANBP2 Knockdown facilitates the Nuclear Reimport of the viral polymerase complex proteins PB1/PB2/PA and**
194 **segment-selective vRNP over-export to the cytoplasm. (A)** A549 cells were transduced with LV shRNA-Control or shRNA-
195 RANBP2 and infected with influenza A virus (IAV) (A/WSN/1933) at MOI 4. At 6h post-infection, protein levels of PB1, PB2, PA
196 and NP were determined by western blot. **(B)** Transduced A549 cells were treated with KPT-330 for 2h and infected with IAV at
197 MOI 0.5. Nucleocytoplasmic fractionation was performed at 6h post-infection and PB1, PB2 and PA levels were determined by
198 western blot (N: nucleus, C: cytoplasm). Lamin and tubulin protein levels were investigated to verify the efficacy of the
199 fractionation. **(C)** Transduced A549 cells were infected with IAV at MOI 0.5 in the absence of KPT-330. The PB1 was stained at

6h post-infection and nuclear fluorescence **(Figure S7)** was quantified using the Fiji software. Each dot represents the nuclear fluorescence of a cell. **(D)** Strand- and segment-specific RTqPCR strategy. Strand-specific reverse transcription (RT) was performed with tagged-primers to amplify separately the genomic viral RNA (vRNA) and the complementary viral RNA (cRNA). Each of the 8 segments of IAV were then amplified by qPCR using specific primers. **(E)** Transduced A549 cells were infected with IAV at MOI 0.5. At 6h post-infection, nuclear (N) and cytoplasmic (C) fractions were separated and total intracellular RNAs were extracted. cRNAs were reverse transcribed by strand-specific RTqPCR and results were normalized on the nuclear fraction of the control condition. **(F)** vRNAs were reverse transcribed by strand-specific RTqPCR and results were normalized on the control condition of each fraction. Results are presented as mean +/- SD.

RANBP2 depletion disrupts the segment stoichiometry by selectively favouring the export of some vRNA segments to the cytoplasm

Having determined that RANBP2 controls Influenza virus replication in the nucleus by regulating the import of the newly synthesised viral polymerase, we asked why the increase in vRNA and vRNP does not translate into an increased production of infectious particles **(Figure 1A)**. To address this, we performed strand-specific RT to distinguish vRNA and cRNA, as previously **(Figure S2A)**, then quantified the 8 IAV segments by qPCR to investigate segment stoichiometry **(Figure 2D, Figure S8A and S8B)**. After sub-cellular fractionation, analysis of viral RNA localization revealed that, while cRNA levels increased for all influenza segments in the nucleus **(Figure 2E)**, segments 1, 2, 3, 7 and 8 exhibited increased vRNA export to the cytoplasm in the absence of RANBP2 compared to other segments **(Figure 2F)**. These findings indicate that, while the depletion of RANBP2 increases the replication of all vRNA segments, it disproportionately affects their export back to the cytoplasm.

Taken together, our results indicated that the knockdown of RANBP2 greatly perturbs infection by IAV, first by facilitating the re-import of polymerase into the nucleus, which increases cRNA and vRNA, second by selectively favouring the export of some vRNA into the cytoplasm. The dysregulation of both these steps may cause an abnormal accumulation of some vRNA segments in the cytoplasm, thus constituting potential pathogen-associated molecular patterns (PAMPs) that may be sensed by the infected cell.

RANBP2 knockdown exacerbates the inflammatory response to IAV infection in primary human macrophages

In ANE1, it is thought that innate immune cells may contribute to the deleterious production of cytokines following IAV infection. To test this in relevant innate immune cells, primary monocytes were isolated from PBMCs from healthy donors and differentiated into pro-inflammatory M1-like macrophages. After 7 days of differentiation, primary monocyte-derived macrophages (MDM) were CD3- CD14+ CD16+ CD11b+ HLA-DR+ CD80- **(Figure S9)**. We first determined that IAV can infect MDMs **(Figure S10A)**, and stimulate an effective immune response without additional pre-stimulation, triggering the synthesis of pro-inflammatory cytokines such as IL-6 and IL-1β **(Figure S10B)**. MDM were then transduced with LVs coding for control or RANBP2 shRNA and infected with IAV **(Figure S1)**. The stimulation of innate immunity was initially assessed by qPCR detection of representative transcripts, namely CXCL10, IL-6, TNFα and IL-1β, comparing MDM with THP-1 and A549 cells. Although some cell-dependent changes were observed, the knockdown of RANBP2 led to a ~2-fold increase in IL-6, up to 6-fold increase in TNFα and IL-1β, and up to 50-fold increase in CXCL10 **(Figure 3A)**, suggesting that RANBP2 regulates the inflammatory response to IAV infection.

To confirm this at the protein level, supernatants were collected at 24 hpi and the secretion of pro-inflammatory mediators was analysed by Multiplex Luminex assay. Strikingly, the knock-down of RANBP2 in primary macrophages led to an exacerbated inflammatory response to IAV infection, with a stronger induction of the pro-inflammatory chemokines CXCL8, CXCL10, CCL2, CCL3 and CCL4 **(Figure 3B)**.

Together, these findings suggest that RANBP2 plays a critical role in modulating the inflammatory response to IAV infection by regulating vRNA replication, nucleocytoplasmic trafficking of viral polymerase subunits,

246 and selective vRNA export. The abnormal accumulation of viral components in the cytoplasm amplifies
247 inflammatory signalling, highlighting a potential mechanism underlying the pathogenesis of ANE.

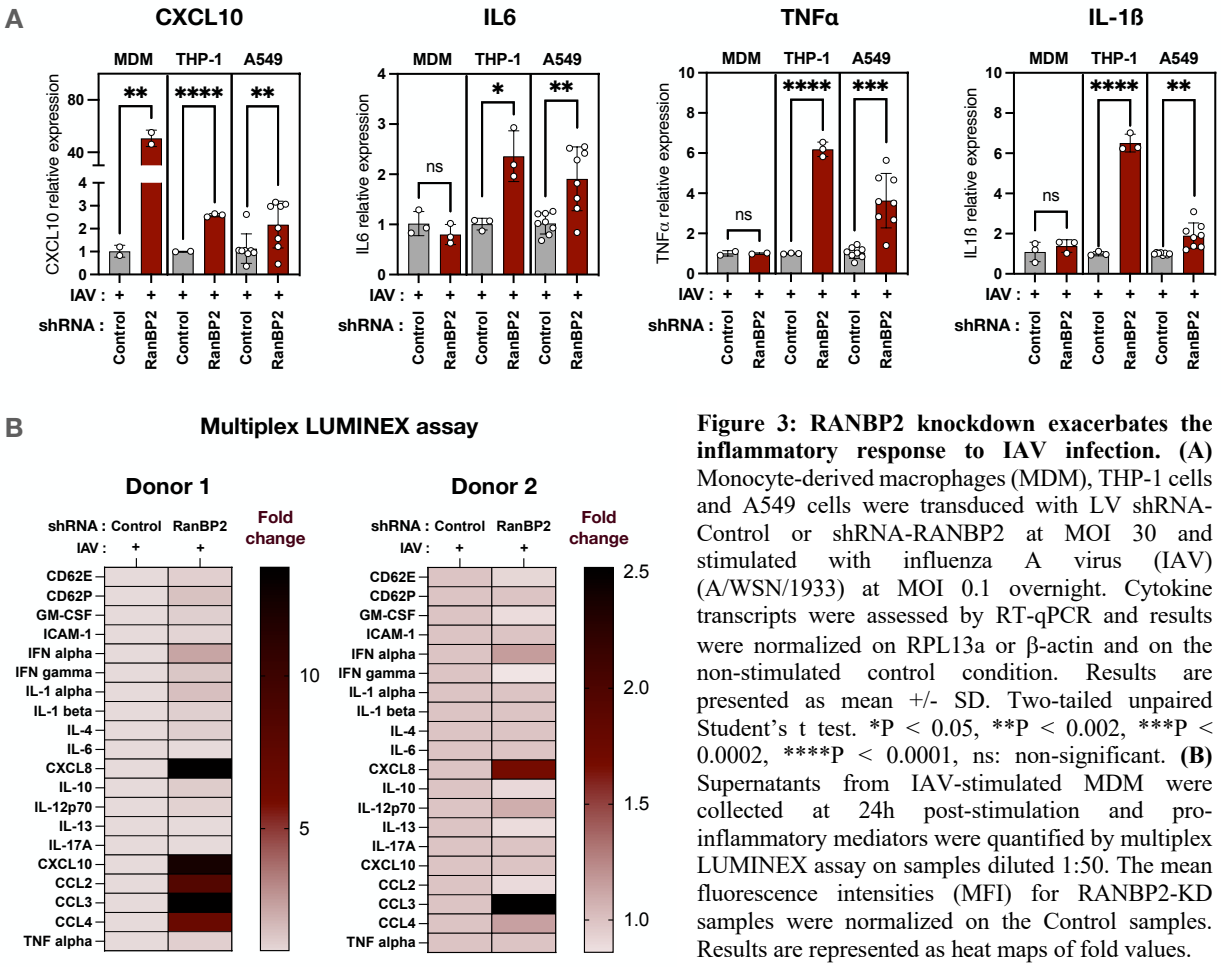

Figure 3: RANBP2 knockdown exacerbates the inflammatory response to IAV infection. (A) Monocyte-derived macrophages (MDM), THP-1 cells and A549 cells were transduced with LV shRNA-Control or shRNA-RANBP2 at MOI 30 and stimulated with influenza A virus (IAV) (A/WSN/1933) at MOI 0.1 overnight. Cytokine transcripts were assessed by RT-qPCR and results were normalized on RPL13a or β-actin and on the non-stimulated control condition. Results are presented as mean +/- SD. Two-tailed unpaired Student's t test. *P < 0.05, **P < 0.002, ***P < 0.0002, ****P < 0.0001, ns: non-significant. **(B)** Supernatants from IAV-stimulated MDM were collected at 24h post-stimulation and pro-inflammatory mediators were quantified by multiplex LUMINEX assay on samples diluted 1:50. The mean fluorescence intensities (MFI) for RANBP2-KD samples were normalized on the Control samples. Results are represented as heat maps of fold values.

248
249 **The RANBP2-T585M ANE1 variant drives hyper-inflammation following IAV infection**

250 Having identified the role of RANBP2 in controlling the IAV-triggered inflammation, we investigated if
251 RANBP2's function is impacted by the predominant ANE-associated mutation. Heterozygous mutations in
252 *RANBP2* are associated with increased susceptibility to acute necrotizing encephalopathy, however it is
253 not known how these affect protein function. Evidence suggests that the disease is not caused by
254 haploinsufficiency, and we previously showed that both alleles, wild-type and mutant, are transcribed in
255 patients (Gouy et al., 2023). However, previous work showed that ANE1 mutations do not alter the
256 structure of RANBP2 (Bley et al., 2022), and that ectopically-expressed RANBP2-T585M still localises to the
257 nuclear envelope (Bley et al., 2022; Shen et al., 2021).

258 We introduced the predominant mutation (c.C1754T, p.T585M), by CRISPR-Cas9 knock-in of U2OS cells
259 **(Figure 4A)**. A total of 47 clones were isolated after puromycin selection during 3 weeks. Mutations were
260 confirmed by allelic qPCR **(Figure 4B, Figure S11A-S11C),** as previously described (Gouy et al., 2023), and
261 by Sanger sequencing of the cDNA **(Figure 4C and 4D)**. For many clones, we noted that CRISPR repair had
262 occurred using the highly homologous RGPD sequences present on the same chromosome (Desgraupes et
263 al., 2023), rather than the repair plasmid, therefore only clones that did not recombine with RGPD were
264 selected **(Figure S11B)**. In total, two wild-type clones (C4 and C15, referred to as WT/WT), one

heterozygously-mutated (C10, WT/C1754T) and three homozygously-mutated (C6, C9 and C14, C1754T/C1754T) clones were isolated.

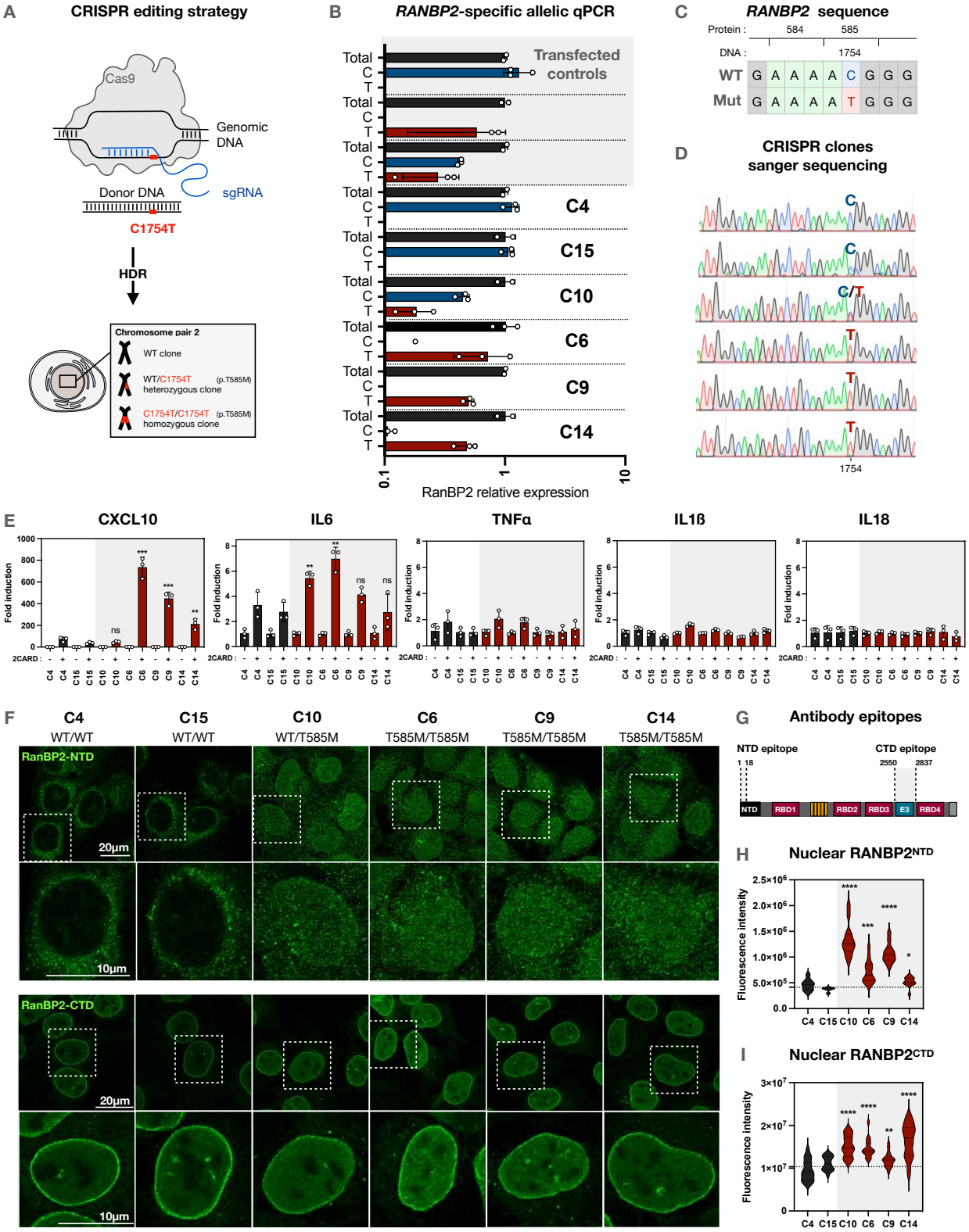

Figure 4: Mislocalisation of the ANE1-mutated N-terminal part of RANBP2 drives hyper-inflammation upon immune stimulation. (A) CRISPR editing strategy. A guide sgRNA hybridizing directly upstream the C1754 position was used to induce the cleavage by the Cas9 enzyme. A donor DNA sequence carrying the C1754T mutation (corresponding to T585M at the protein level) was supplied. After homology directed repair (HDR), three types of CRISPR clones were generated (box below): (top) WT homozygous clones (middle) WT/C1754T heterozygous clones and (bottom) C1754T/C1754T homozygous clones. **(B)** RNA expression of the WT or C1754T form of RANBP2 was assessed by RANBP2-specific RTqPCR. HEK-293T cells transfected with plasmids encoding the WT form, the T585M form or both forms of RANBP2 were used as control. **(C)** Illustration of the RANBP2 sequence from positions 1749 to 1757, carrying a C on the WT sequence at position 1754, replaced by a T on the T585M mutant. **(D)** Sanger sequencing of the CRISPR clones showing either a C, a T or both at position 1754. **(E)** CRISPR clones were stimulated by transfection with the 2CARD module of RIG-I or untransfected (-), and total intracellular RNAs were extracted at 24h post-transfection. Pro-inflammatory cytokine expression was assessed by RTqPCR to detect CXCL10, IL6, TNFα, IL1β and IL18 transcripts. Values were normalized on RPL13a and for the untransfected control condition. Results are presented as mean +/- SD. Two-tailed unpaired Student's t test. *P < 0.05, **P < 0.002, ***P < 0.0002, ****P < 0.0001, ns: non-significant. **(F)** CRISPR clones were fixed and stained for RANBP2 using either an antibody recognizing the NTD (amino acids 1 to 18) or the CTD (amino acids 2550 to 2837) parts of RANBP2. **(G)** Schematic representation of the RANBP2 protein sequence and the epitopes recognized by the antibodies. Nuclear fluorescence was quantified using the Fiji software for **(H)** $RANBP2^{NTD}$ and **(I)** $RANBP2^{CTD}$.

Since U2OS cells are not stimulated by IAV infection **(Figure S12)**, we transfected cells with the constitutive 2-CARD (caspase recruitment domain) of the retinoic acid-inducible gene I (RIG-I), as used previously (Maarifi et al., 2018). Activation of innate immune pathways was measured by qPCR and normalised for house-keeping genes. The transfection of the 2-CARD domain stimulated the expression of the inflammatory transcripts IL-6 and CXCL10, and this was significantly exacerbated in clones stably expressing the ANE1 disease variant **(Figure 4E)**. In particular, homozygous ANE1 mutations led to a ~2-3-log increase in CXCL10 transcription following stimulation, suggesting that the ANE1 disease variant exacerbates innate immune responses to agonist stimulation.

In CRISPR-Cas9 knock-in cells, $RANBP2^{NTD}$ mislocalises away from nuclear pores

Although previous work indicated that ectopically-expressed RANBP2-T585M still localizes to the NPC (Bley et al., 2022; Shen et al., 2021), no CRISPR knock-in cell lines have been generated. We therefore examined the localisation of RANBP2 by immunofluorescence in the clones expressing RANBP2-T585M heterozygously and homozygously. Using a well-characterized antibody that recognises $RANBP2^{NTD}$ of the protein (amino acids 1-18, Pierce PA1-082)(Di Nunzio et al., 2012), we observed that, while RANBP2 was localised at the nuclear envelope in WT clones, as expected, its localisation was diffuse throughout the cell in all ANE1 clones **(Figure 4F-4G)**. Intriguingly, however, using an antibody that recognises the CTD of the protein (amino acids 2550-2837 (Wu et al., 1995)) resulted in a detection of the protein at the nuclear envelope for all clones **(Figure 4F)**. These results suggested that in ANE1 cells, the NTD of RANBP2 is no longer retained at the nuclear envelope.

Taken together, our results suggest that the presence of the NTD of RANBP2 at the nuclear envelope is critical to safeguard cells from the pathological inflammation following viral infection. In ANE1, mutations in the NTD of RANBP2 are specifically associated with hyperinflammation.

DISCUSSION

In this work, we show that the NPC component RANBP2 regulates the nucleocytoplasmic transport of Influenza A virus proteins and RNAs. Its absence from nuclear pores contributes to exacerbated viral replication in the nucleus, and a disproportionate increase in some viral RNAs. While previous work indicated that RANBP2 is a co-factor for the infection by some viruses (Bichel et al., 2013; Di Nunzio et al., 2012; Schaller et al., 2011; Zhang et al., 2010; Copeland et al., 2009; Hofemeister and O'Hare, 2008), this study reveals an opposite role in IAV infection, namely the restriction of key nuclear transport steps.

RANBP2 can regulate the nucleocytoplasmic transport of macromolecules by two major mechanisms, first by regulating the cycle of Ran, second by interacting with nuclear transport receptors (Yokoyama et al., 1995; Hutten et al., 2008). The replication of IAV involves four distinct sequential NCT steps, namely the

import of incoming vRNPs, the export of viral mRNAs, the import of translated viral proteins, and the export of vRNPs. RANBP2 was found to regulate only two of these steps, suggesting a specific mechanism. In particular, RANBP2 was not involved in the initial entry of incoming vRNPs into the nucleus, which involves the classical karyopherin α/β nuclear import pathway (Miyake et al., 2019; Nguyen et al., 2023; Dou et al., 2018), nor in the initial export of viral transcripts, which involves the general mRNA export pathway via NXF1:NXT1. Rather, RANBP2 acted on late nuclear transport steps of IAV, after translation of the viral proteins. First, RANBP2 was found to regulate the re-import of the polymerase complex subunits, which is known to involve different pathways, the best characterised being via the β-karyopherin RanBP5 (Huet et al., 2010; Hemerka et al., 2009; Cros et al., 2005). Second, results suggest that RANBP2 exerts a quality control checkpoint for vRNAs that are exported back to the cytoplasm, a step known to depend on the β-karyopherin CRM1 (Elton et al., 2001; Ma et al., 2001; Watanabe et al., 2001). Our results therefore suggest that RANBP2 may impact viral NCT by interacting with key β-karyopherins.

Despite increased vRNA levels, infectious viral particle production did not increase. Our results indicated that the absence of RANBP2 disrupted the segment stoichiometry, leading to the disproportionate increase in the largest segments (1, 2, 3), and in segments that undergo splicing (7 and 8). Changes in segment stoichiometry could lead to packaging defects, however, the mechanism responsible for this imbalance in viral RNA export is not known. It is possible that the increase in vRNA corresponds to truncated RNA segments, especially since large deletions are frequent in the segments coding for PB1, PB2 and PA.

After replication, Influenza viral genomic single stranded RNA molecules are sensed by RIG-I, which results in the production of pro-inflammatory cytokines downstream of NF-κB (Iwasaki and Pillai, 2014). In the absence of RANBP2, IAV infection led to a dramatic increase in the pro-inflammatory response, especially with the production of chemokines. We hypothesize that the disproportionate increase of some cRNA/vRNA segments in the cytoplasm could constitute PAMPs that exacerbate the inflammatory response.

Influenza viruses are responsible for the majority of ANE1 cases in children. The high prevalence for Influenza over other respiratory infections (e.g., RSV, SARS-CoV-2) and childhood febrile illnesses (e.g., streptococcal infections) is puzzling and unexplained. Our work suggests that, by restraining key steps of IAV nucleocytoplasmic trafficking, RANBP2 is responsible for limiting the accumulation of viral PAMPs in the cytoplasm. Additionally, in CRISPR knock-in cells expressing the ANE1 disease variant, stimulation of innate immune signalling downstream of RIG-I led to a high expression of some pro-inflammatory transcripts, indicating that RANBP2 also regulates innate immune signalling. Although the prevalent phenotype was observed in homozygously edited cells, this is the first demonstration that ANE1 mutation is associated with exacerbated inflammation. This role of RANBP2 in controlling innate immunity is coherent with the symptoms observed in ANE1 patients as they express elevated levels of pro-inflammatory cytokines.

It remains unclear how heterozygous dominant single point mutations in the NTD of RANBP2 contribute to disease. Previous work suggests that both wild-type and mutant alleles are expressed in patients (Gouy et al., 2023), suggesting that the mutant allele might have dominant negative activity. However, ANE1 mutations were shown not to affect protein structure, nor localisation at the NPC using ectopically-expressed RANBP2 (Bley et al., 2022; Shen et al., 2021). In CRISPR knock-in cells, we demonstrate that the T585M mutation in the NTD causes its redistribution away from the nuclear envelope. This change was observed in both homozygously and heterozygously-edited cells, confirming a dominant negative activity of the T585M mutant. Future work is needed to determine how the relocalisation of RANBP2 contributes to disease. Intriguingly, however, the change was observed with an antibody targeting the NTD, but not with an antibody targeting the CTD, suggesting that the full-length RANBP2 still localises at the nuclear

pores. Thus, the mutation does not affect the ability of mutant-RANBP2 to anchor into the NPCs but might induce the generation of truncated forms of RANBP2 (lacking at least amino acids 2550 to 2837). Future work in patient samples will be essential to determine whether ANE1 mutations favour the accumulation of RANBP2 isoforms or truncated forms.

SUPPLEMENTARY FIGURES

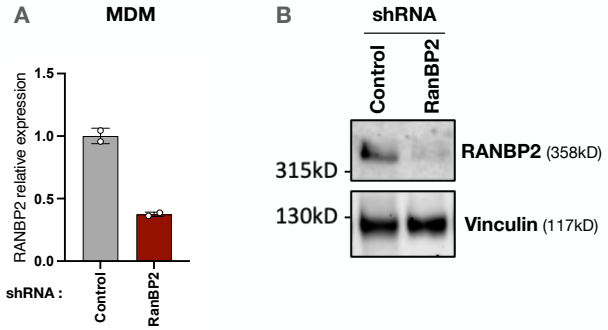

Figure S1: Assessment of RANBP2 knock-down in human primary macrophages and A549 cells. (A) Monocyte-derived macrophages (MDM) were transduced with LV shRNA-Control or shRNA-RANBP2 at MOI 20. Knock-down efficacy was assessed by RTqPCR at 24h post-infection **(B)** Knock-down efficacy was confirmed by Western blot in A549 cells at 72h post-infection.

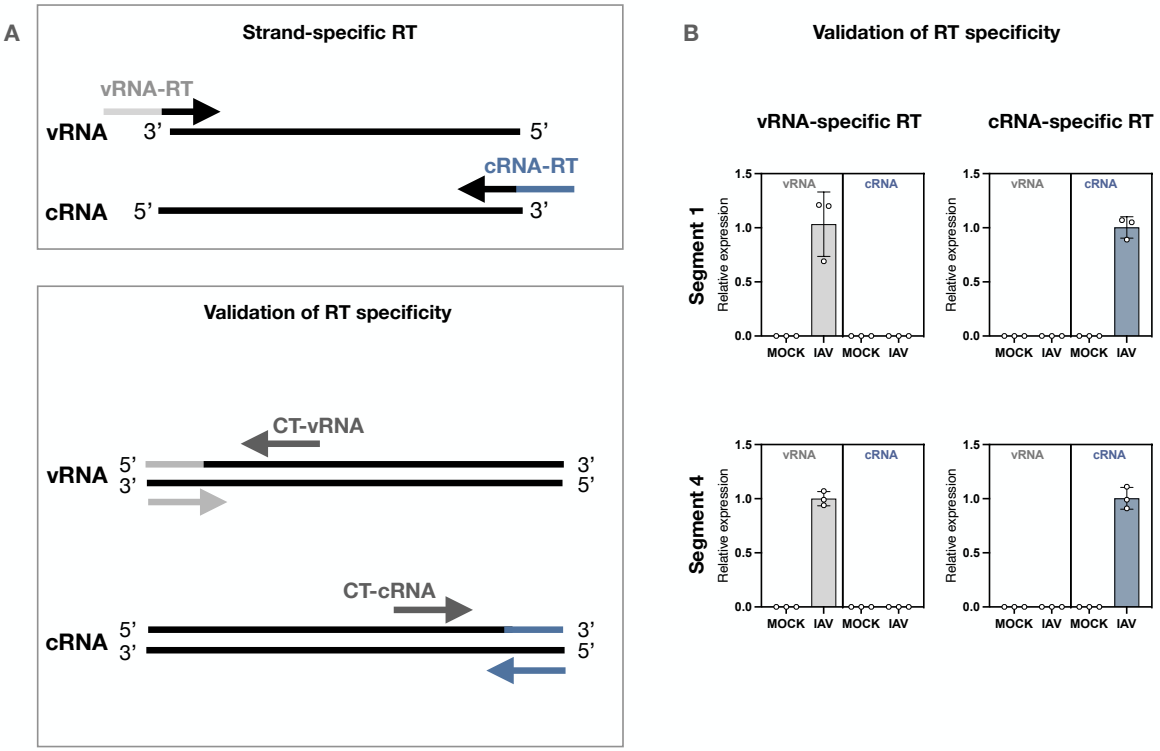

Figure S2: RT-qPCR strategy to distinguish cRNA and vRNA. (A) Strand-specific Reverse Transcription (RT) strategy. Genomic viral RNAs (vRNA) and complementary RNAs (cRNA) were reverse transcribed using specific tagged-primers hybridizing to the consensus 3'-sequences of each of the 8 viral segments. **(B)** Validation of the specificity of the strand-specific RT. qPCR primers complementary to the tags were used to amplify cDNAs produced by each RT and verify that only vRNAs were

379 amplified after vRNA-specific RT, only cRNAs after cRNA-specific RT and no cellular RNAs were reverse transcribed by any of
380 the two RT. RT-specificity was check for 2 segments (segment 1 and segment 4).

Additionnal images for Figure 1G

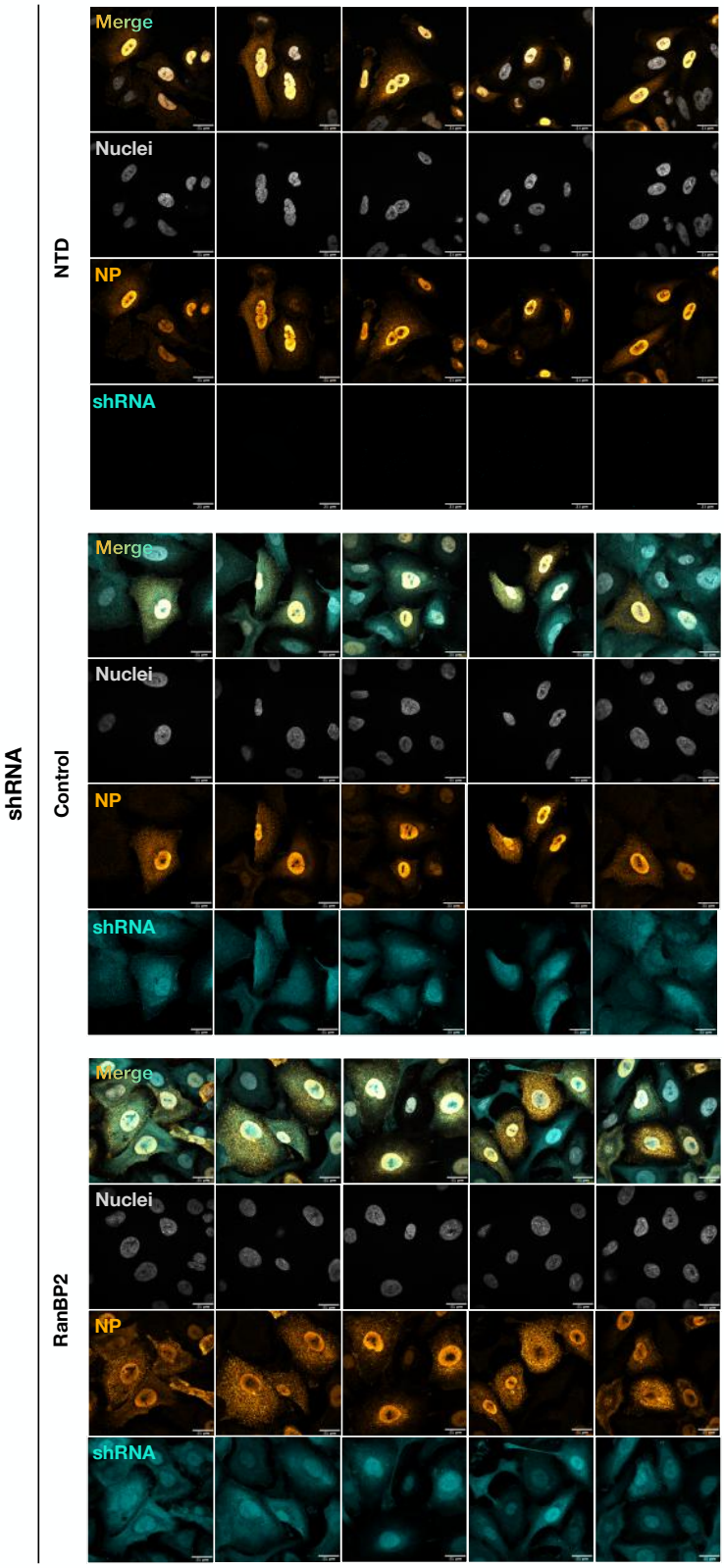

Figure S3: Increase in cytoplasmic NP in RANBP2-KD cells at 8 hpi. Full panel of images for Figure 1G. A549 cells were transduced or not (NTD) with LV shRNA-Control or shRNA-RANBP2 and infected with influenza A virus (IAV) (A/WSN/1933) at MOI 0.5. At 8h post-infection, cells were fixed and stained for the nucleoprotein (NP). Scale bar: 20µm. Image processing was done using the Fiji software. NP (AlexaFluor-488) and shRNA (mCherry) colors were changed to « Orange Hot » and « cyan » for aesthetic purposes.

381

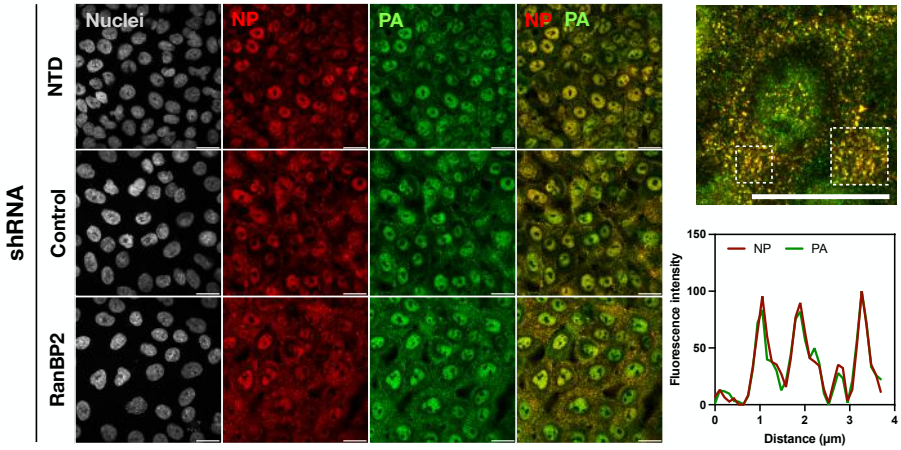

Figure S4: Increase in cytoplasmic vRNP in RANBP2-KD cells at 8 hpi. Transduced A549 cells were infected at MOI 0.5 and co-stained for the NP and PA proteins at 8h post-infection. Scale bar: 20µm. Colocalization was quantified using the Fiji software.

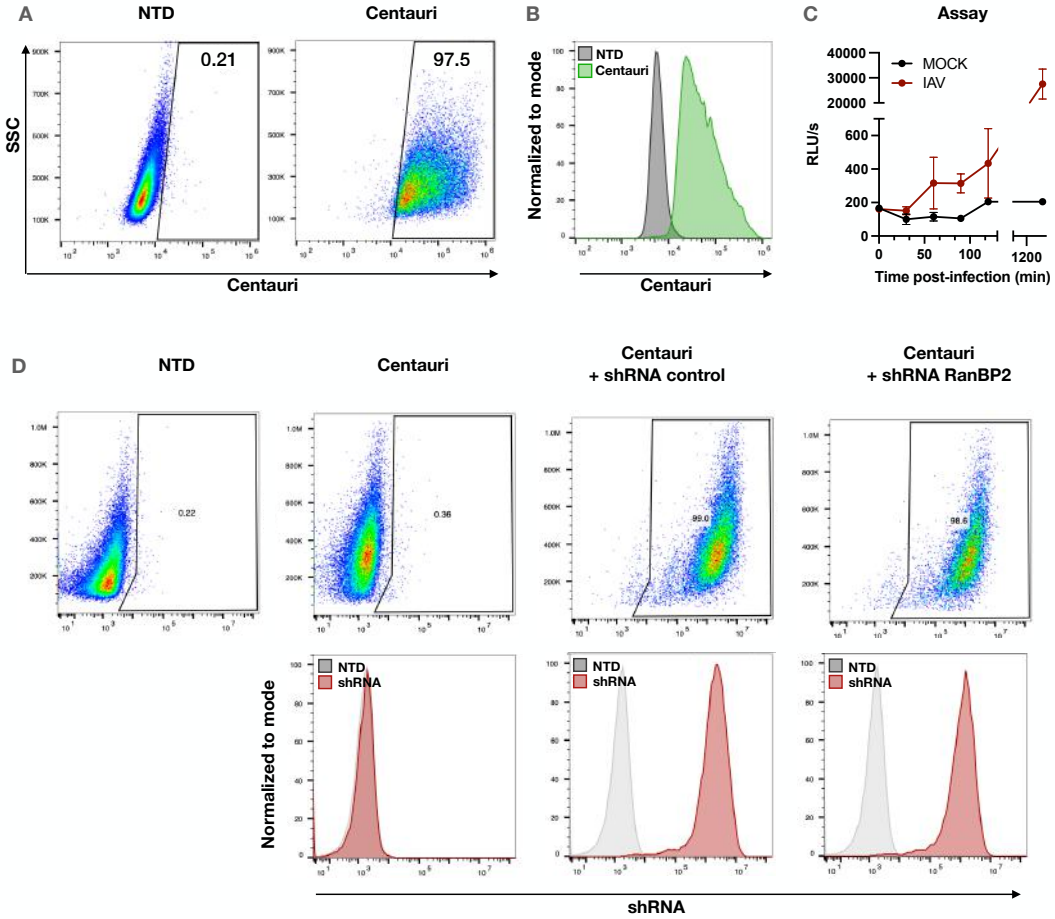

Figure S5: Alpha-Centauri assay to measure IAV nuclear import. (A-B) A549 cells were transduced with a plasmid containing the Centauri-Nluc tagged with HA. Cells were stained for the HA and analyzed by flow cytometry to determine the percentage of transduced cells. **(C)** Cells were infected at MOI 4 and the luminescence was measured to assess the Nanoluciferase complementation upon nuclear import of the viral ribonucleoproteins. **(D)** Centauri-Nluc-transduced A549 cells were transduced with LV shRNA-Control or shRNA-RANBP2 expressing the mCherry. The percentage of mCherry-positive cells was determined by flow cytometry.

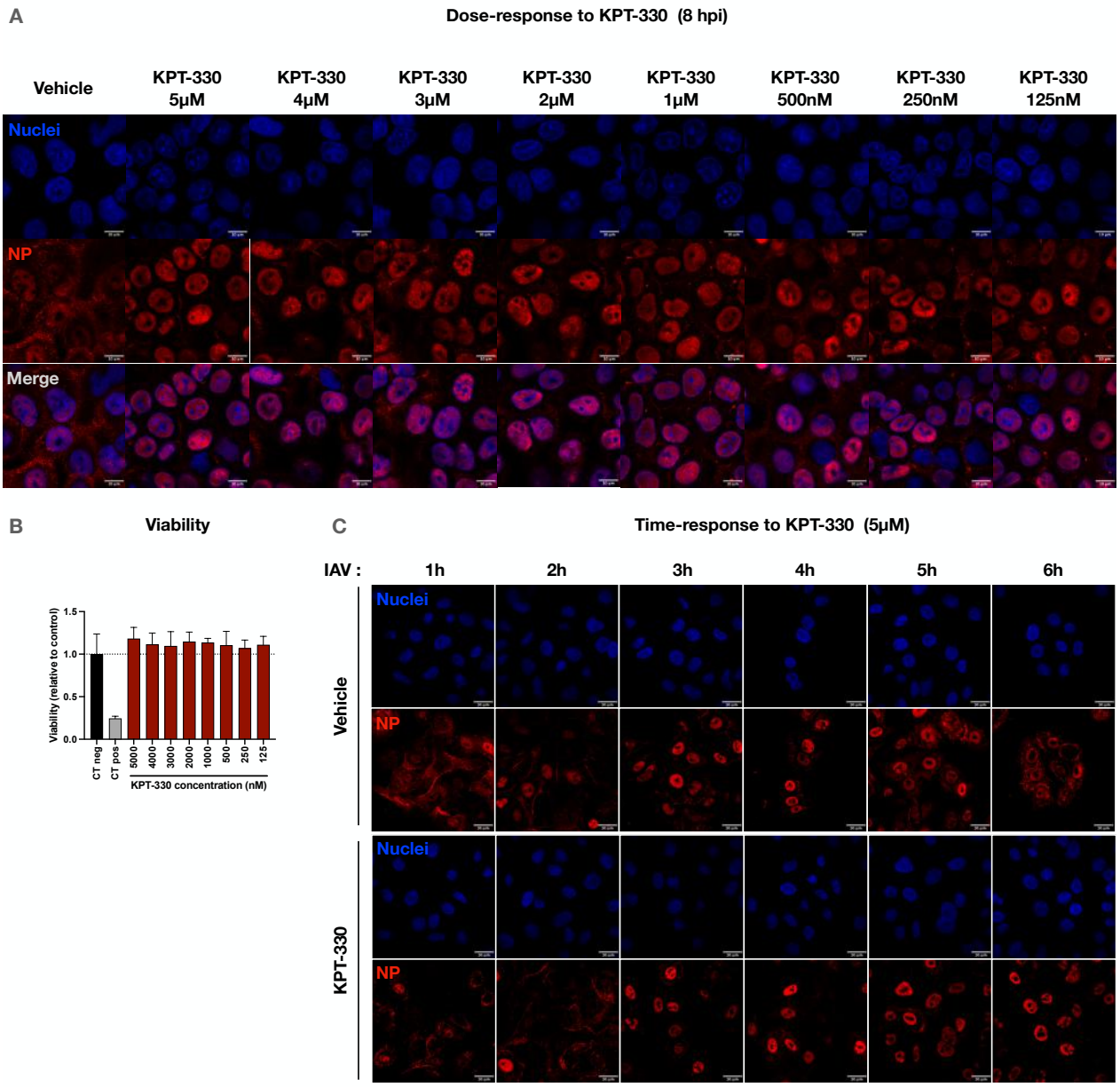

Figure S6: Inhibition of CRM1-dependent NP export using KPT-330/Selinexor. A549 cells were treated or not (Vehicle) with KPT-330 at the indicated doses for 2 h at 37°C, then infected with IAV. **(A)** Cells were fixed and stained for the NP at 8 hour post-infection (hpi) to verify the efficacy of the NP export inhibition. **(B)** KPT-330 cytotoxicity was assessed by MTT assay. Uninfected cells were incubated with MTT (5 mg/mL) for 3 h at 37°C. Acid isopropanol was added and absorbance was read at 570nm. **(C)** At the indicated times post-infection, cells were fixed and stained for the NP to determine when vRNP export starts.

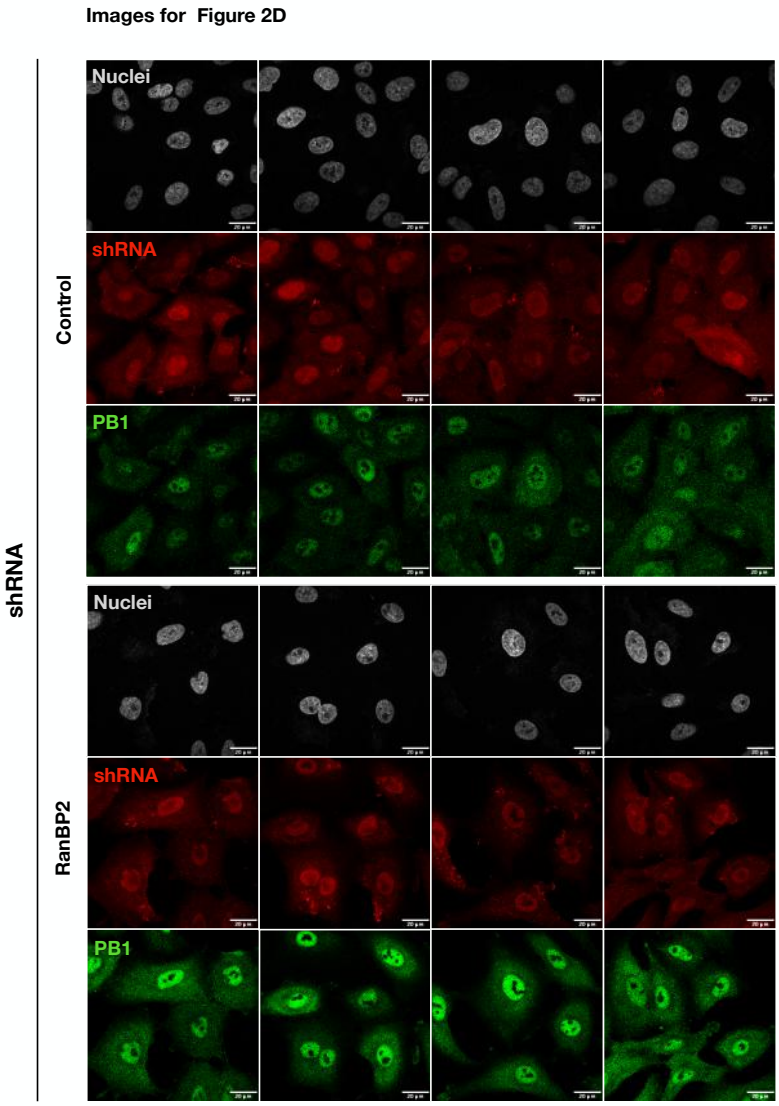

Figure S7: Increase in nuclear PB1 in RANBP2-KD cells. Full panel of images for Figure 2D. A549 cells were transduced with LV shRNA-Control or shRNA-RANBP2 and infected with influenza A virus (IAV) (A/WSN/1933) at MOI 0.5. At 6h post-infection, cells were fixed and the PB1 protein was stained. Scale bar: 20µm. Image processing was done using the Fiji software.

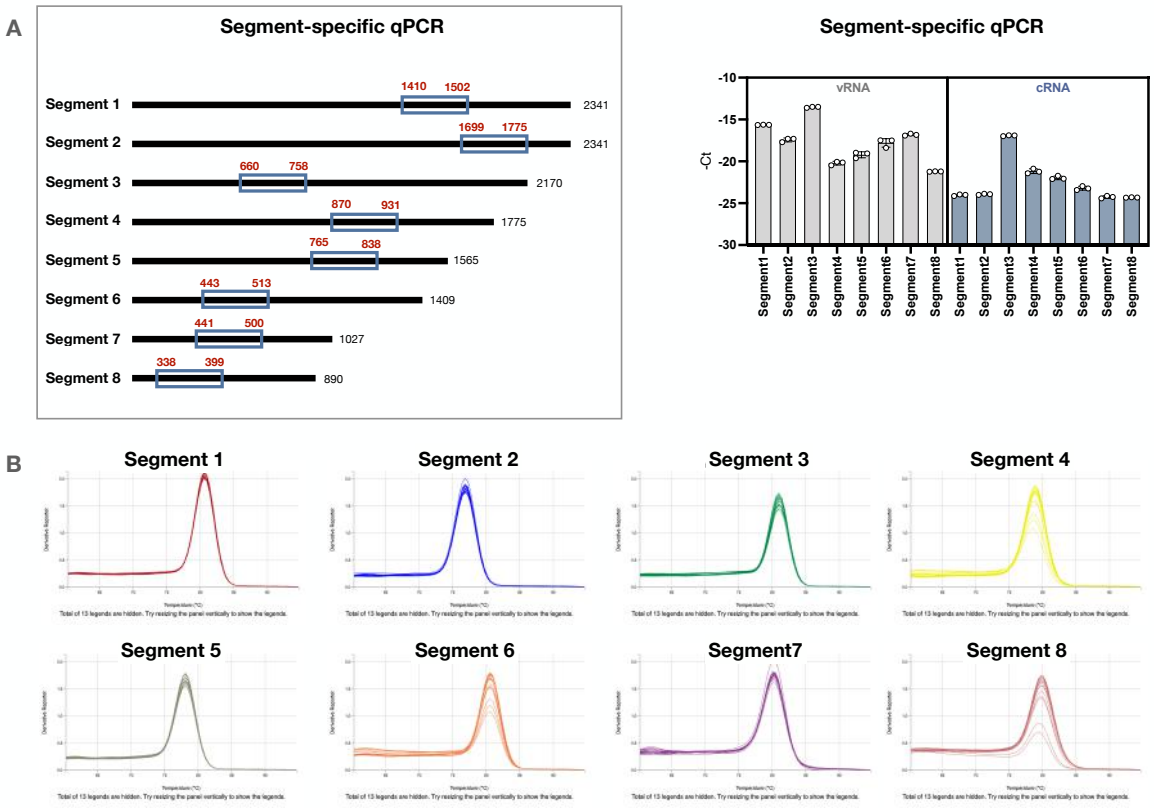

Figure S8: qPCR strategy to amplify the 8 segments of IAV. (A) Segment-specific qPCR strategy. After strand-specific RT, the 8 segments were detected using qPCR primers amplifying the indicated regions of each segments. All 8 segments were amplified after each RT. **(B)** Segment-specific qPCR was performed after total RT (amplifying all RNAs) and all primer pairs were still specific of the viral RNA segments. Melting curves are presented.

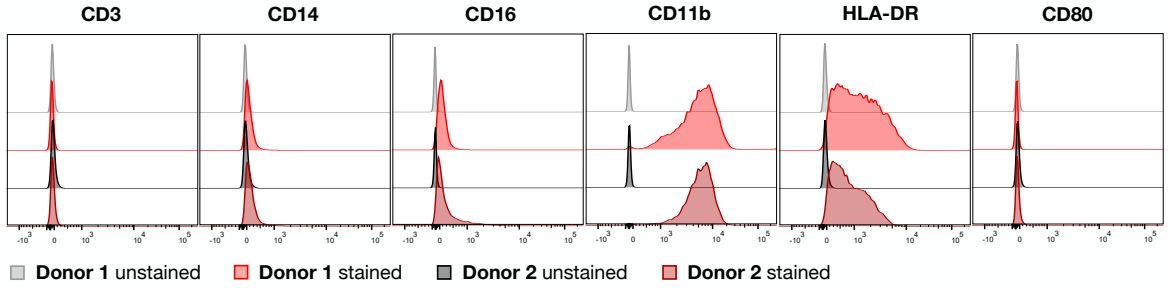

Figure S9: Phenotypic analysis of primary human MDM. PBMCs were isolated from blood samples of two healthy donors. Monocytes were isolated by plastic adherence for 45 minutes and differentiated into macrophages by addition of GM-CSF. After 7 days of differentiation, monocyte-derived macrophages from 2 donors were stained for phenotypic markers. The expression of CD3, CD14, CD16, CD11b, HLA-DR and CD80 was assessed by flow cytometry.

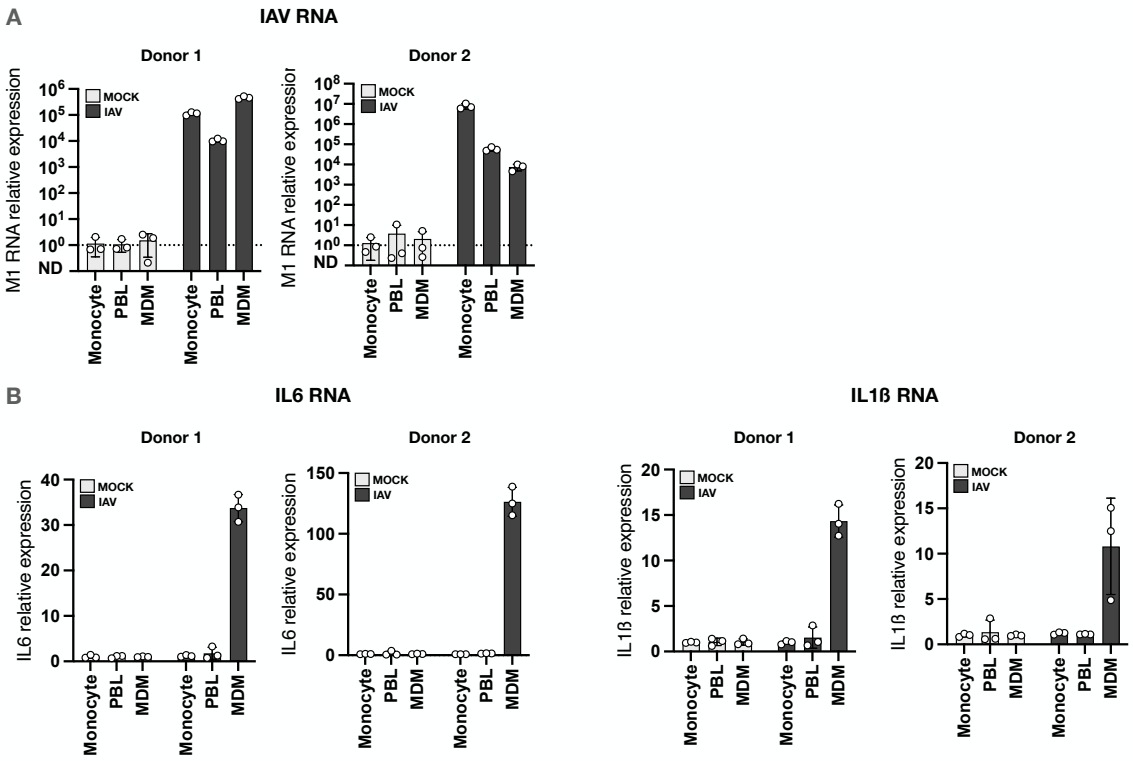

Figure S10: Stimulation of MDM with IAV triggers IL-6 and IL-1β synthesis. PBMCs were isolated from blood samples of two healthy donors. Monocytes were isolated by plastic adherence for 45 minutes. Supernatants containing the peripheral blood lymphocytes (PBL) were collected. Macrophages were differentiated by addition of GM-CSF to monocytes for 7 days at 37°C. Each cell types was infected with influenza A virus (IAV) (A/WSN/1933) at MOI 0.5. At 16h post-infection, total intracellular RNAs were extracted. **(A)** M1-encoding viral RNAs were amplified by RTqPCR. (**B)** IL-6 and IL-1ß RNAs were amplified by RTqPCR. Results are presented as mean +/- SD and normalized on the non-infected condition for each cell type.

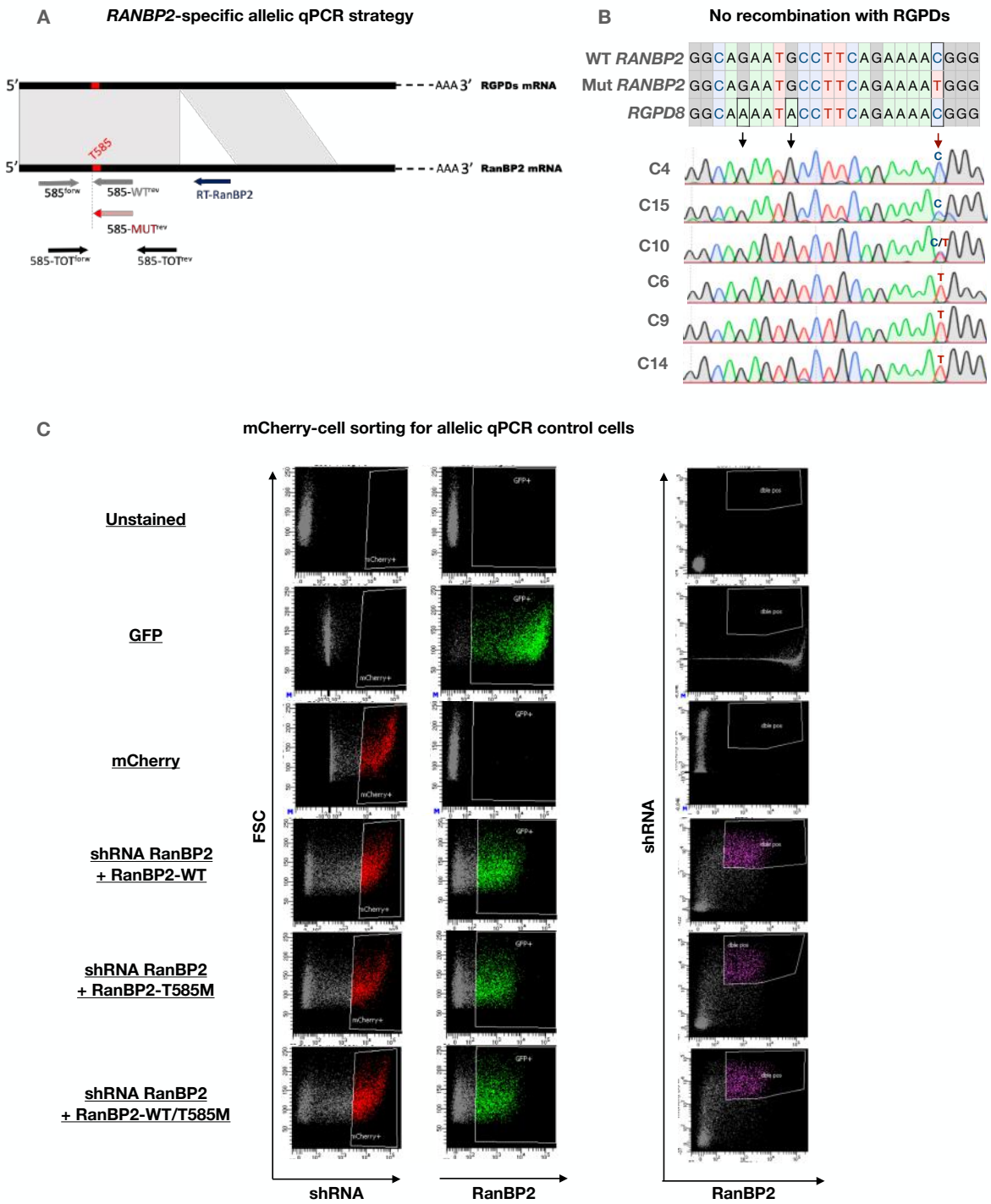

Condition	% mCherry-positive cells	% GFP-positive cells	% double-positive cells	Nb of cells after sorting
NTF	0	0	0	200000
GFP	0,1	90,9	0	N/A
mCherry	35,7	0	0	N/A
Ran + WT	25	37,4	24,8	106440
Ran + T585M	26,1	31,6	17,8	69272
Ran + WT/T585M	33,2	33,7	21,4	133453

Figure S11: CRISPR-Cas9 knock-in strategy to generate ANE1-variants in U2OS cells. (A) RANBP2-specific allelic qPCR strategy. RANBP2-specific reverse transcription was performed using a primer specific to the RANBP2 sequence and not present on the highly homologous RGPD sequence (conserved parts are indicated in gray). Mutant and WT RANBP2 were distinguished

428 using a reverse qPCR primer carrying either an A or a G at its 3' end. A set of primers was also designed to amplify RANBP2 (near
429 the same region) without distinguishing both forms. **(B)** Representation of the RANBP2 sequence upstream of the repair site, and
430 one of the eight RGPDs. Sanger sequencing of the CRISPR clones shows no recombination with the RGPD sequence as all carry a
431 G at the indicated positions (black arrows). **(C)** To produce controls for the screening of CRISPR clones by allelic qPCR, HEK-
432 293T cells were transfected with mCherry-shRNA-RANBP2 and either GFP-RANBP2-WT, GFP-RANBP2-T585M or both.
433 mCherry-expressing cells were sorted by FACS and total intracellular RNAs were extracted for the allelic RTqPCR. Results of the
434 FACS sorting are presented.

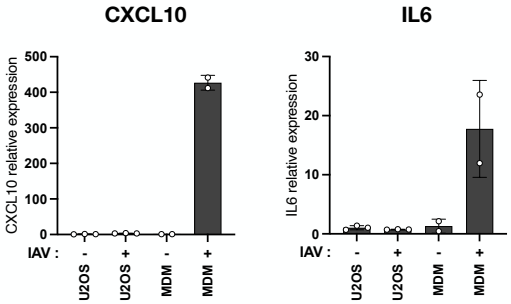

435

436 **Figure S12: U2OS cells are not stimulated by IAV infection.** U2OS cells or monocyte-derived macrophages (MDM) were
437 infected with influenza A virus (IAV) (A/WSN/1933) at MOI 0.5. At 16h post-infection, total intracellular RNAs were extracted
438 and the expression of CXCL10 and IL-6 was assessed by RTqPCR.
439

440 **SUPPLEMENTARY TABLES**

Plasmids	
Target	Reference
pVSVg	pHCMV-G (Yee et al., PNAS 1994)
p8.74	pCMVΔR8.74 (Dull et al., J Virol 1998)
mCherry-shRNA-Control	Addgene #1864 (Gouy et al., Front Neurol 2023)
mCherry-shRNA-RanBP2	Gouy et al., Front Neurol 2023
GFP-RanBP2-WT	Gift from J Joseph (Pune University)
GFP-RanBP2-T585M	This paper, availbale upon request
Centauri-Nluc-NLS	This paper, availbale upon request

441

442 **Table S1: List of plasmids.**

Reverse transcription primers

IAV strand-specific RT	
Target	Sequence (5' -> 3')
vRNA	GGCCGTCATGGTGGCGAATAGCGAAAGCAGG
cRNA	CCAGATCGTTCGAGTCGTAGTAGAAACAAGG

The colored sequence corresponds to the tag

RanBP2-specific RT	
Target	Sequence (5' -> 3')
RanBP2	ATGCTGTTGGGGTGGAAGCC

qPCR primers

Target	Forward primer (5'-3')	Reverse primer (5'-3')
IAV M1	CAGCACTGGAGCTAGGATGA	AAGGCTATGGAGCAAATGGC
IAV NP	CCTCGGGCCAAATCAGCATA	ATTCCCAGTGAATGCTGCCA
Segment 1	CGGGATATTGCCCGACATGA	TCCGCGCTGGAATACTCATC
Segment 2	TACCGGTGCCATAGAGGTGA	TGGGTTTGCTCCCACAGTTT
Segment 3	CAAGCTTGCCGACCAAAGTC	TTGCCCTCAATGTAGCCGTT
Segment 4	GGCATCATCACCTCAAACGC	CCCTGGGGTGTTTGACACTT
Segment 5	TCAAGTGAGAGAGAGCCGGA	TGAGTGCAGACCGTGCTAAA
Segment 6	TTAATGAGCTGCCCTGTCGG	GCTGACCAAGCAACCGATTC
Segment 7	CCACTGAAGTGGCATTTGGC	GCTGGGAGTCAGCAATCTGT
Segment 8	GCTCATGCCCAAGCAGAAAG	CCATGATCGCCTGGTCCATT
RanBP2 (Total)	AAAACATGGCCTTCAACCTG	TCAACAATTTCTGATGCCTGA
RanBP2 (WT)	TGGGATGCGGTTTGTACTCT	AGAATTAAGACCGCTGCCCG
RanBP2 (T585M)	TGGGATGCGGTTTGTACTCT	AGAATTAAGACCGCTGCCCA
RanBP2 (Exon24)	CAGGAAGCTCAAAAATCTCAGACA	ACCATCACTTCAGTCCCACC
IL-6	TAACCACCCCTGACCCAACC	ATTTGCCGAAGAGCCCTCAG
IL-1ß	GGCATCCAGCTACGAATCTC	GAACCAGCATCTTCCTCAGC
TNFα	GGCGTGGAGCTGAGAGATAAC	GGTGTGGGTGAGGAGCACAT
IL-18	GGAATTGTCTCCCAGTGCAT	ACTGGTTCAGCAGCCATCTT
CXCL10	GTCCACGTGTTGAGATCATTGC	TTGCTCCCCTCTGGTTTTAAGG
RPL13a	AACAGCTCATGAGGCTACGG	TGGGTCTTGAGGACCTCTGT
β-actin	CTGGAACGGTGAAGGTGACA	AAGGGACTTCCTGTAACAATGCA

Table S2: List of reverse transcription and qPCR primers.

Antibodies			
Immunofluorescence			
Target	Reference	Brand	Dilution
NP	MCA400	Biorad	1/1000
PB1	GTX125923	GeneTex	1/500
RANBP2	PA1-O82	Pierce	1/100
RANBP2		Gift from R Wozniak	1/1000
Goat anti-Mouse AF488	A11001	Thermofisher Scientific	1/1000
Goat anti-Rabbit AF488	A11034	Thermofisher Scientific	1/1000
Goat anti-Mouse AF555	A21424	Thermofisher Scientific	1/1000
Flow cytometry and MDM phenotyping			
Target	Reference	Brand	Dilution
HA (Centauri)	11988506001	Roche, Sigma	1/100
CD3-BV421 (clone UCHT1	300433	Biolegend	1/100
CD14-PerCP-Cy5.5 (clone HCD14)	325621	Biolegend	1/100
CD16-Alexa700 (clone 3G8)	302026	Biolegend	1/100
CD11b-APC-Cy7 (clone M1/70)	101225	Biolegend	1/100
HLA-DR-FITC (REA805)	130-111-941	Miltenyi	1/100
CD80-BV650 (clone 2D10)	305227	Biolegend	1/100
Western Blot			
Target	Reference	Brand	Dilution
NP	MCA400	Biorad	1/5000
PB1	GTX125923	GeneTex	1/5000
PB2	GTX125925	GeneTex	1/5000
PA	GTX125932	GeneTex	1/5000
Pro-IL1ß	16806-1-AP	Proteintech	1/1000
NLRP3	AG-20B-0014	Adipogen	1/1000
Actin ß	A1978	Roche, Sigma	1/3000
Lamin A/C	10298-1-AP	Proteintech	1/400
Tubulin	ab6160	Abcam	1/5000
Goat anti-Mouse HRP	NA931V	GE Healthcare	1/5000
Donkey anti-rabbit HRP	NA934V	GE Healthcare	1/5000

Table S3: List of antibodies.

MATERIALS & METHODS

Viruses, lentiviral vectors and cells

Infections with IAV were carried out with the H1N1/A/WSN/1933 strain in all experiments except for the Alpha-Centauri assay where this same strain was engineered to express a fragment of the NanoLuc (IAV-alpha) as described below. Lentiviral vectors (LV) were produced by transfecting HEK-293T cells in calcium phosphate with a pVSVg plasmid, an encapsidation Gag-Pol plasmid (p8.74) and the plasmid of interest (i.e. mCherry-shRNA-Control, mCherry-shRNA-RANBP2 or Centauri-NLuc-NLS) (see **Table S1** for plasmid information). After 48 h, vectors were harvested and ultracentrifuged for 1 h at 22,000 rpm (Optima XE-90, Beckman Coulter) at 4°C. A549 cells (ATCC) and CRISPR U2OS clones (homemade) were cultured in Dulbecco's Modified Eagle Medium (DMEM, Gibco) containing 10% of Fetal bovine serum (FBS, Serana) and 1× penicillin/streptomycin (PS, Gibco) at 37°C with 5% CO2. THP-1 cells and monocyte-derived macrophages (MDM) were cultured in Roswell Park Memorial Institute (RPMI-1640, Gibco) medium containing 10% FBS and 1× of PS.

IAV infections

Cells were infected with IAV at MOI 0.5 in all experiments, except when monitory the early steps of the viral cycle (i.e. internalization, nuclear import), when MOI 4 was used to increase signal detection. Cells were exposed to IAV for 1 h in a small volume of 2% FBS culture medium to promote viral adsorption at the cell surface before replacing viral inoculum with warm culture medium and incubation at 37°C with 5% CO2. For experiments with NF-κB canonical pathway inhibition, cells were pre-treated with 2% FBS culture medium containing 20 µM of PS1145 (MedChemExpress) for 1 h at 37°C.

469 **RNA extractions and RTqPCR**

470 Intracellular RNAs were extracted using the RNeasy mini kit (Qiagen) according to the manufacturer's
471 protocol. RNA yields and purity were assessed by spectrophotometry (NanoDrop 2000c, Thermofisher
472 Scientific). Unspecific reverse transcription (RT) was performed using the PrimeScript RT Reagent Kit
473 (Perfect Real Time, Takara Bio Inc.) with random and polyT primers. IAV strand-specific RT was performed
474 using tagged primers that bind either to the consensus 3'-end sequence of vRNAs (all 8 segments) or to
475 the consensus 3'-end sequence of cRNAs (all 8 segments as well) with Superscript III (Invitrogen,
476 Thermofisher Scientific) in the presence of DTT 0.1M (Invitrogen, Thermofisher Scientific), dNTP 10mM
477 (Invitrogen, Thermofisher Scientific) and RNAsin (Promega). Distinction between segments was then made
478 using specific qPCR primers (**Table S2**). RANBP2-specific RT was performed using a primer (at 1µM) that
479 binds to RANBP2 on a sequence absent from RGPDs, as published in (Gouy et al., 2023) PrimeScript RT
480 Reagent Kit was used (Perfect Real Time, Takara Bio Inc.) (**Table S2**). Real-time quantitative PCR was
481 performed using the Power Up kit (Applied Biosystems, Thermofisher Scientific) on the ViiA7 thermocycler
482 (Life technologies, Thermofisher Scientific). All qPCR primers are listed in **Table S2**.

483 **Immunofluorescence**

484 Cells were washed with PBS and fixed with 4% paraformaldehyde (PFA, Thermofisher Scientific) for 10 min
485 at room temperature (R/T). After 3 PBS washes, remaining PFA was neutralized with PBS containing 50mM
486 of NH4Cl for 10 min at R/T. After 2 PBS washes, cells were permeabilized using PBS containing 0.5% of
487 Triton-100X (Sigma-Aldrich) for 15 min at R/T. Cells were washed twice in PBS and saturated in PBS
488 supplemented with 2% of Normal goat serum (NGS, Invitrogen, Thermofisher Scientific). Primary stainings
489 were performed for 1h at R/T with antibodies listed in **Table S3**. Cells were washed 5 times with PBS and
490 secondary antibodies were added for 30 min at R/T (**Table S3**). After 5 PBS washes, cells were stained with
491 Hoechst (Thermofisher Scientific) diluted to the 1/10,000 in PBS for 5 min at R/T. Cells were washed 5
492 times with PBS and mounted in Prolong Diamond anti-fade mounting medium (Invitrogen, Thermofisher
493 Scientific). Imaging was carried out using the Confocal Zeiss LSM880 Airyscan microscope of the
494 Montpellier Ressources Imagerie (MRI) platform. Image processing and quantifications were done using
495 the Fiji software (2.14.0): Alexafluor-488 staining of the NP was changed to the color « Orange Hot » for
496 aesthetic purposes and brightness was increased uniformly in all conditions. Full panels of images are
497 provided in supplementary data.

498 **Alpha-Centauri assay**

499 Cloning steps. A DNA fragment coding for αNluc (GVTGWRLCERILA) flanked by NotI and NheI overhangs
500 was obtained by annealing two overlapping oligonucleotides:

NotI-αNLuc-NheI-F GGCCGCAGGGGGAGTGACAGGGTGGAGACTATGCGAAAGAATACTTGCATAAG

NotI-αNLuc-NheI-R CTAGCTTATGCAAGTATTCTTTCGCATAGTCTCCACCCTGTCACTCCCCCTGC

501 The reverse genetics plasmid pPolI-SL-PB2-αNluc was obtained by subcloning this restriction fragment
502 between the NotI and NheI sites of the pPolI-SL-PB2-Nanoluc described in Diot 2016.

503 Particle production by reverse genetics. The eight pPolI-WSN-PB2-αNluc, -PB1, -PA, -HA, -NP, -NA, -NS, -
504 M, and four pcDNA3.1-WSN-PB2, -PB1, -PA, -NP plasmids (0.5 µg of each) were co-transfected into a co-
505 culture of 293T and MDCK cells (seeded in a 6-well plate at 4×10^5 and 3×10^5 cells, respectively) using 10
506 µL of FuGENE® HD transfection reagent (Promega). After 24 h of incubation at 35°C, cells were washed
507 twice with DMEM and incubated in DMEM containing 1 µg/mL of TPCK-treated trypsin for 48 h. The
508 reverse genetics supernatant was titrated on MDCK by plaque assay and the recombinant PB2-αNluc virus

509 was amplified at an MOI of 10^{-4} on MDCK cells for 3 days at 35°C. The viral stock was titrated on MDCK by
510 plaque assays and sequenced to verify the presence of the αNluc coding sequence.

511 Cells were transduced with LV Centauri-NLuc-NLS for 3 days, then with LV shRNA-Control or LV shRNA-
512 RANBP2 at MOI 15 for 4 days. Cells were then infected with IAV-α at MOI 4 for the indicated times.
513 NanoGlo live cell substrate (Promega) was added and luminescence was measured with the Infinite M Plex
514 spectrophotometer (Tecan).

515 **Nucleo-cytoplasmic fractionation**

516 Nuclear and cytoplasmic fractions were separated using the NE-PER Kit (Thermofisher Scientific) according
517 to the manufacturer's protocol. Briefly, 1-2 million cells were washed with PBS then lysed in cold CER I
518 buffer, vortexed 15 seconds and incubated on ice for 10 min. Cold CER II buffer was then added and cells
519 were vortexed 5 seconds then incubated on ice for 1 min. After 5 second vortex and full speed
520 centrifugation, supernatants (cytoplasmic fraction) were harvested and stored at -80°C. Pellets (nuclei)
521 were resuspended in cold NER buffer and 4 cycles of 15 second vortex then 10-min incubation on ice were
522 performed. After full speed centrifugation, supernatants (nuclear fraction) were harvested and stored at -
523 80°C.

524 **Western blot**

525 Cell lysates were sonicated for 20 cycles of 30 seconds ON, 30 seconds OFF (Bioruptor Pico, Diagenode)
526 and 4X Laemmli (250 mM Tris-HCl pH 7, 8% sodium dodecyl sulphate (SDS), 40% glycerol, 10% β-
527 mercaptoethanol and 0.005% bromophenol blue) was added. After denaturation at 95°C for 5 min,
528 samples underwent SDS polyacrylamide gel electrophoresis (SureCast Gel Handcast System, Thermo Fisher
529 Scientific) and were transferred on a 0.45 µm nitrocellulose membrane (Sigma Aldrich). Membranes were
530 saturated in PBS containing 0.05% Tween 20 (Sigma) and 10% milk powder for 30 min. Primary antibodies
531 were added and left overnight at 4°C (**Table S3**). After 3 PBS washes, secondary antibodies were added for
532 1 h at R/T (**Table S3**). Protein revelation was carried out by measuring HRP activity (Immobilon Forte
533 Western HRP substrate, Merck) with a Chemidoc imager (Biorad).

534 **TCID50 assay**

535 MDCK cells were washed in FBS-free MEM medium (Gibco) and serially diluted cell supernatants were
536 added in 2% FBS in octoplicates. After 3 days at 37°C and 5% CO2, cells were washed twice in PBS and fixed
537 with 4% PFA for 10 min at R/T. Violet crystal was added, washed twice in water and cytopathic effect was
538 observed. The TCID50 titer was determined using the formula:

539 $\log10 (TCID50/mL) = x0 - (d/2) + (d*xi/n) + v$

540 x0: decimal logarithm of initial dilution factor.

541 d: decimal logarithm of serial dilution factor.

542 xi: score of positive events.

543 n: number of replicates.

544 v: decimal logarithm of the inoculum volume (mL).

545 **Peripheral blood mononuclear cell (PBMC) isolation**

546 Buffy coats from healthy donors were obtained from the Établissement Français du Sang (EFS). Whole
547 blood was diluted by half with Phosphate buffered saline (PBS) and loaded on an equivalent volume of
548 Lymphoprep (Stemcell technologies) at R/T. Tubes were centrifuged at 800g for 30 min at 20°C without
549 brakes. The PBMC ring was collected using a 5 mL pipet and washed 3 times in a final volume of 50 mL of

PBS (centrifugations at 1200 rpm for 5 min at 20°C with brakes on). The cell pellet was resuspended in 30 mL of 10% FBS RPMI-1640 medium. PBMCs were counted manually using counting chambers (Kova).

Monocyte-derived macrophages differentiation

After PBMC isolation, 20 million cells were seeded per well into 6-well plates and incubated for 45 min, at 37°C with 5% CO2. After monocyte adherence, cells were washed 3 times with 10% FBS RPMI-1640 medium directly on the cell layers to remove non-attached cells. For monocyte-derived macrophage (MDM) differentiation, monocytes were cultured in 10% FBS RPMI-1640 medium containing GM-CSF (50 ng/mL, Gentaur) for 8 days.

Flow cytometry phenotyping

After 8 days of MDM differentiation, phenotypic markers were analysed by flow cytometry on a Fortessa using the following antibodies: CD3-BV421 (clone UCHT1, Biolegend 300433), CD14-PerCP-Cy5.5 (clone HCD14, Biolegend 325621), CD16-Alexa700 (clone 3G8, Biolegend 302026), CD11b-APC-Cy7 (clone M1/70, Biolegend 101225), HLA-DR-FITC (REA805, Miltenyi 130-111-941), and CD80-BV650 (clone 2D10, Biolegend 305227).

Multiplex LUMINEX assay

The presence of mediators of inflammation was assessed in supernatants of stimulated cells using the ProcartaPlex Human inflammation Panel 20-plex kit (Invitrogen, ThermoFisher Scientific). A few samples were centrifuged and diluted to the 1/10 or to the 1/50 in order to determine optimal dilution for the experiment. Dilution to the 1/50 was chosen to detect the strongly induced mediators (e.g. IL-8) in the range of the standard curves supplied in the kit. Buffers and standards were prepared according to the manufacturer's protocol. Briefly, Capture Bead mix was vortexed and added to the plate, washed in Wash buffer, then samples and standards were added. The plate was incubated 1 h at R/T on a shaker. After 2 washes, Biotinylated Detection Antibody mix was added for 30 min at R/T on a shaker. After 2 washes, Streptavidin-PE was added for 30 min at R/T on a shaker. After 2 more washes, the plate was read on the MAGPIX flow cytometer (LUMINEX).

Establishment of U2OS clones expressing RANBP2 T585M by CRISPR knock-in

The plasmid pUcIDT Amp (synthetized by Integrated DNA Technologies) containing the donor sequences (see below) and the plasmid pSpCas9(BB)-2A-Puro (PX459) (Addgene #62988) modified to contain the guide sequences (GGCAGAATGCCTTCAGAAAA) were co-transfected at equal quantity in the human osteosarcoma cell lines U2OS using Lipofectamine 3000 (Invitrogen, ThermoFisher Scientific) following the manufacturer's instructions. Two days post-transfection, cells were selected using puromycin (Gibco) at 2µg/ml during four days. The different clones were established by limiting dilution. A total of 198 cells were split in 576 different wells containing 10% FBS DMEM medium. After 3 weeks, 47 clones were established and analyzed by RANBP2-specific RTqPCR as describe above and Sanger sequencing (Eurofins).

<u>Donor DNA sequence</u>:

(GCGGTTTGTACTCTGATTCACAGAAAAGCAGTgtaagtagtaaaacaaaaatattgctttcacttagtgcgtaggttttaccggggattt
aatcctcatgtgaagatttaatttgtcatgtgacccattaacatatatgtatgtaagccctgaactgtgtatttagaaagcaattttagtaaattgaactat
tttttagACCTGGAAACGTAGCAAAATTGAGACTTCTAGTTCAGCATGAAATAAACACTCTAAGAGCCCAGGAAAAAC
ATGGCCTTCAACCTGCTCTGCTTGTACATTGGGCAGA<u>g</u>TG<u>t</u>CT<u>g</u>CAGAAAA<u>t</u>Ggtgagttttaaagtataagcatttttaaagaa
cattaccttaatttttttaaaatcatgaactttttattgaaagtttttttgttctgaaaacagcagcttggtcacattatgacagatgtgtttttttattgctgca
aaatagttaatgtagttaaatataagcacttagaggagcaatgcctggcacacagtgaatgttacatattagctgagctgttactgttattccttaataat
taagttctgataattattcagcctgaaaattaaaaaaa)

Capital letters: exon

593 lowercase: intron

594 underlined: mutations

595 Bold lowercase: C1754T mutation

596 **Generation of homozygous/heterozygous RANBP2-expressing control cells for allelic qPCR**

597 HEK-293T cells were transfected with plasmids encoding the mCherry-RanBP2-shRNA and either GFP-
598 RANBP2-WT, GFP-RANBP2-T585M or both (**Table S1**) in calcium phosphate. After 48 h of culture, cells
599 were detached using trypsin (Gibco) and sorted on the ARIA IIu cytometer (Becton Dickinson) of the MRI
600 platform to isolate the mCherry-positive cells. Sorted cells were lyzed and total RNAs were extracted using
601 the RNeasy mini kit (Qiagen) according to the manufacturer's protocol.

602 **Statistical analysis**

603 Statistical analysis was performed using the GraphPad Prism software (10.2.3).

604 **ACKNOWLEDGMENTS**

605 This work was financed by grants from the Agence Nationale pour le Recherche (ANR-23-CE15-0005-01)
606 and ANRS-MIE (ECTZ209411). We thank Marion Cannac (Université de Montpellier, France) for help with
607 phenotyping primary macrophages, and Montpellier Ressources Imagerie (MRI) for support with flow
608 cytometry, cell sorting and imaging. We thank Rick Wozniak (University of Alberta, Canada) for the kind
609 gift of RANBP2-specific antibody, Jomon Joseph (National Center for Cell Science, Pune, India) for the GFP-
610 RANBP2 construct, and Sébastien Nisole (INSERM) for the GFP-RANBP2-T585M construct.

611 **REFERENCES**

612 Bartolini, L., S. Ricci, C. Azzari, M. Moriondo, F. Nieddu, M. L'Erario, Z. Ricci, G. Simonini, M.
613 Mortilla, G. Indolfi, C. Montagnani, E. Chiappini, L. Galli, and R. Guerrini. 2024. Severe
614 A(H1N1)pdm09 influenza acute encephalopathy outbreak in children in Tuscany, Italy,
615 December 2023 to January 2024. *Eurosurveillance*. 29. doi:10.2807/1560-
616 7917.ES.2024.29.17.2400199.

617 Bashiri, F.A., S. Al Johani, M.H. Hamad, A.Y. Kentab, A.H. Alwadei, K. Hundallah, H.H. Hasan, W.
618 Alshuaibi, L. Jad, M.T. Alrifai, A. Hudairi, R. Al Sheikh, A. Alenizi, N.A. Alharthi, T.A.
619 Abdelmagid, D. Ba-Armah, M.A. Salih, and B. Tabarki. 2020. Acute Necrotizing
620 Encephalopathy of Childhood: A Multicenter Experience in Saudi Arabia. *Front. Pediatr.*
621 8:526. doi:10.3389/fped.2020.00526.

622 Bichel, K., A.J. Price, T. Schaller, G.J. Towers, S.M. Freund, and L.C. James. 2013. HIV-1 capsid
623 undergoes coupled binding and isomerization by the nuclear pore protein NUP358.
624 *Retrovirology*. 10:81. doi:10.1186/1742-4690-10-81.

625 Bley, C.J., S. Nie, G.W. Mobbs, S. Petrovic, A.T. Gres, X. Liu, S. Mukherjee, S. Harvey, F.M. Huber,
626 D.H. Lin, B. Brown, A.W. Tang, E.J. Rundlet, A.R. Correia, S. Chen, S.G. Regmi, T.A.
627 Stevens, C.A. Jette, M. Dasso, A. Patke, A.F. Palazzo, A.A. Kossiakoff, and A. Hoelz. 2022.
628 Architecture of the cytoplasmic face of the nuclear pore. *Science*. 376:eabm9129.
629 doi:10.1126/science.abm9129.

630 Carlon-Andres, I., F. Lagadec, N. Pied, F. Rayne, M.-E. Lafon, R.H. Kehlenbach, and H. Wodrich.
631 2020. Nup358 and Transportin 1 Cooperate in Adenoviral Genome Import. *J. Virol.*
632 94:e00164-20. doi:10.1128/JVI.00164-20.

633 Carter, T., and M. Iqbal. 2024. The Influenza A Virus Replication Cycle: A Comprehensive Review.
634 *Viruses*. 16:316. doi:10.3390/v16020316.

635 Chatur, N., C. Yea, B. Ertl-Wagner, and E.A. Yeh. 2022. Outcomes in influenza and *RANBP2*
636 mutation-associated acute necrotizing encephalopathy of childhood. *Dev. Med. Child*
637 *Neurol.* 64:1008–1016. doi:10.1111/dmcn.15165.

638 Clohisey, S., and J.K. Baillie. 2019. Host susceptibility to severe influenza A virus infection. *Crit.*
639 *Care*. 23:303. doi:10.1186/s13054-019-2566-7.

640 Copeland, A.M., W.W. Newcomb, and J.C. Brown. 2009. Herpes Simplex Virus Replication: Roles
641 of Viral Proteins and Nucleoporins in Capsid-Nucleus Attachment. *J. Virol.* 83:1660–1668.
642 doi:10.1128/JVI.01139-08.

643 Cros, J.F., A. García-Sastre, and P. Palese. 2005. An Unconventional NLS is Critical for the Nuclear
644 Import of the Influenza A Virus Nucleoprotein and Ribonucleoprotein. *Traffic*. 6:205–
645 213. doi:10.1111/j.1600-0854.2005.00263.x.

646 Desgraupes, S., L. Etienne, and N.J. Arhel. 2023. RANBP2 evolution and human disease. *FEBS*
647 *Lett.* 597:2519–2533. doi:10.1002/1873-3468.14749.

648 Di Nunzio, F., A. Danckaert, T. Fricke, P. Perez, J. Fernandez, E. Perret, P. Roux, S. Shorte, P.
649 Charneau, F. Diaz-Griffero, and N.J. Arhel. 2012. Human Nucleoporins Promote HIV-1
650 Docking at the Nuclear Pore, Nuclear Import and Integration. *PLoS ONE*. 7:e46037.
651 doi:10.1371/journal.pone.0046037.

652 Dou, D., R. Revol, H. Östbye, H. Wang, and R. Daniels. 2018. Influenza A Virus Cell Entry,
653 Replication, Virion Assembly and Movement. *Front. Immunol.* 9:1581.
654 doi:10.3389/fimmu.2018.01581.

655 Elton, D., M. Simpson-Holley, K. Archer, L. Medcalf, R. Hallam, J. McCauley, and P. Digard. 2001.
656 Interaction of the Influenza Virus Nucleoprotein with the Cellular CRM1-Mediated
657 Nuclear Export Pathway. *J. Virol.* 75:408–419. doi:10.1128/JVI.75.1.408-419.2001.

658 Fernandez, J., C. Hassen-Khodja, V. Georget, T. Rose, Y. Jacob, Y.L. Janin, S. Nisole, P.-O. Vidalain,
659 and N.J. Arhel. 2021. Measuring the subcellular compartmentalization of viral infections
660 by protein complementation assay. *Proc. Natl. Acad. Sci.* 118:e2010524118.
661 doi:10.1073/pnas.2010524118.

662 Fodor, E., and A.J.W. Te Velthuis. 2020. Structure and Function of the Influenza Virus
663 Transcription and Replication Machinery. *Cold Spring Harb. Perspect. Med.* 10:a038398.
664 doi:10.1101/cshperspect.a038398.

665 Gounder, A.P., and A.C.M. Boon. 2019. Influenza Pathogenesis: The Effect of Host Factors on
666 Severity of Disease. *J. Immunol. Baltim. Md 1950*. 202:341–350.
667 doi:10.4049/jimmunol.1801010.

668 Gouy, B., A. Decorsière, S. Desgraupes, W. Duan, H. Ouyang, Y.E. Wang, E.A. Yeh, A.F. Palazzo,
669 T.J. Moraes, S. Nisole, and N.J. Arhel. 2023. Rapid and inexpensive bedside diagnosis of
670 RAN binding protein 2-associated acute necrotizing encephalopathy. *Front. Neurol.*
671 14:1282059. doi:10.3389/fneur.2023.1282059.

672 Hemerka, J.N., D. Wang, Y. Weng, W. Lu, R.S. Kaushik, J. Jin, A.F. Harmon, and F. Li. 2009.
673 Detection and Characterization of Influenza A Virus PA-PB2 Interaction through a
674 Bimolecular Fluorescence Complementation Assay. *J. Virol.* 83:3944–3955.
675 doi:10.1128/JVI.02300-08.

676 Hofemeister, H., and P. O'Hare. 2008. Nuclear pore composition and gating in herpes simplex
677 virus-infected cells. *J. Virol.* 82:8392–8399. doi:10.1128/JVI.00951-08.

678 Huet, S., S.V. Avilov, L. Ferbitz, N. Daigle, S. Cusack, and J. Ellenberg. 2010. Nuclear Import and
679 Assembly of Influenza A Virus RNA Polymerase Studied in Live Cells by Fluorescence
680 Cross-Correlation Spectroscopy. *J. Virol.* 84:1254–1264. doi:10.1128/JVI.01533-09.

681 Hutten, S., A. Flotho, F. Melchior, and R.H. Kehlenbach. 2008. The Nup358-RanGAP Complex Is
682 Required for Efficient Importin α/β-dependent Nuclear Import. *Mol. Biol. Cell*. 19:2300–
683 2310. doi:10.1091/mbc.e07-12-1279.

684 Iwasaki, A., and P.S. Pillai. 2014. Innate immunity to influenza virus infection. *Nat. Rev. Immunol.*
685 14:315–328. doi:10.1038/nri3665.

686 Jiang, J., Y.E. Wang, A.F. Palazzo, and Q. Shen. 2022. Roles of Nucleoporin RanBP2/Nup358 in
687 Acute Necrotizing Encephalopathy Type 1 (ANE1) and Viral Infection. *Int. J. Mol. Sci.*
688 23:3548. doi:10.3390/ijms23073548.

689 Joseph, J., and M. Dasso. 2008. The nucleoporin Nup358 associates with and regulates
690 interphase microtubules. *FEBS Lett.* 582:190–196. doi:10.1016/j.febslet.2007.11.087.

691 Khanna, M., K. Sharma, S.K. Saxena, J.G. Sharma, R. Rajput, and B. Kumar. 2024. Unravelling the
692 interaction between Influenza virus and the nuclear pore complex: insights into viral
693 replication and host immune response. *VirusDisease*. 35:231–242. doi:10.1007/s13337-
694 024-00879-6.

695 Koh, J.C., A. Murugasu, J. Krishnappa, and T. Thomas. 2019. Favorable Outcomes With Early
696 Interleukin 6 Receptor Blockade in Severe Acute Necrotizing Encephalopathy of
697 Childhood. *Pediatr. Neurol.* 98:80–84. doi:10.1016/j.pediatrneurol.2019.04.009.

698 Lee, V.W.M., T.B. Khoo, C.M. Teh, H.S. Heng, L. Li, Y.L.M. Yusof, N.A. Yahaya, S. Dharshini, S.W.
699 Wong, T. Nickson, and ANE Malaysia Outcome Study Group. 2023. Factors associated

700 with outcomes of severe acute necrotizing encephalopathy: A multicentre experience in
701 Malaysia. *Dev. Med. Child Neurol.* 65:1256–1263. doi:10.1111/dmcn.15536.

702 Levine, J.M., N. Ahsan, E. Ho, and J.D. Santoro. 2020. Genetic Acute Necrotizing Encephalopathy
703 Associated with RANBP2: Clinical and Therapeutic Implications in Pediatrics. *Mult. Scler.*
704 *Relat. Disord.* 43:102194. doi:10.1016/j.msard.2020.102194.

705 Li, J., L. Su, J. Jiang, Y.E. Wang, Y. Ling, Y. Qiu, H. Yu, Y. Huang, J. Wu, S. Jiang, T. Zhang, A.F.
706 Palazzo, and Q. Shen. 2023. RanBP2/Nup358 Mediates Sumoylation of STAT1 and
707 Antagonizes Interferon-α-Mediated Antiviral Innate Immunity. *Int. J. Mol. Sci.* 25:299.
708 doi:10.3390/ijms25010299.

709 Ma, K., A.-M.M. Roy, and G.R. Whittaker. 2001. Nuclear Export of Influenza Virus
710 Ribonucleoproteins: Identification of an Export Intermediate at the Nuclear Periphery.
711 *Virology*. 282:215–220. doi:10.1006/viro.2001.0833.

712 Maarifi, G., J. Fernandez, D.M. Portilho, A. Boulay, J. Dutrieux, S. Oddos, G. Butler-Browne, S.
713 Nisole, and N.J. Arhel. 2018. RanBP2 regulates the anti-retroviral activity of TRIM5α by
714 SUMOylation at a predicted phosphorylated SUMOylation motif. *Commun. Biol.* 1:193.
715 doi:10.1038/s42003-018-0198-0.

716 Mettelman, R.C., and P.G. Thomas. 2021. Human Susceptibility to Influenza Infection and Severe
717 Disease. *Cold Spring Harb. Perspect. Med.* 11:a038711.
718 doi:10.1101/cshperspect.a038711.

719 Miyake, Y., J.J. Keusch, L. Decamps, H. Ho-Xuan, S. Iketani, H. Gut, U. Kutay, A. Helenius, and Y.
720 Yamauchi. 2019. Influenza virus uses transportin 1 for vRNP debundling during cell entry.
721 *Nat. Microbiol.* 4:578–586. doi:10.1038/s41564-018-0332-2.

722 Mizuguchi, M., H. Yamanouchi, T. Ichiyama, and M. Shiomi. 2007. Acute encephalopathy
723 associated with influenza and other viral infections. *Acta Neurol. Scand.* 115:45–56.
724 doi:10.1111/j.1600-0404.2007.00809.x.

725 Munier, S., T. Rolland, C. Diot, Y. Jacob, and N. Naffakh. 2013. Exploration of Binary Virus–Host
726 Interactions Using an Infectious Protein Complementation Assay. *Mol. Cell. Proteomics*.
727 12:2845–2855. doi:10.1074/mcp.M113.028688.

728 Neilson, D.E., R.M. Eiben, S. Waniewski, C.L. Hoppel, M.E. Varnes, B.A. Bangert, M. Wiznitzer,
729 M.L. Warman, and D.S. Kerr. 2003. Autosomal dominant acute necrotizing
730 encephalopathy. *Neurology*. 61:226–230. doi:10.1212/01.WNL.0000073544.28775.1A.

731 Nguyen, N.L.T., W. Wu, and N. Panté. 2023. Contribution of the Nuclear Localization Sequences
732 of Influenza A Nucleoprotein to the Nuclear Import of the Influenza Genome in Infected
733 Cells. *Viruses*. 15:1641. doi:10.3390/v15081641.

734 Okumura, A., M. Mizuguchi, H. Kidokoro, M. Tanaka, S. Abe, M. Hosoya, H. Aiba, Y. Maegaki, H.
735 Yamamoto, T. Tanabe, E. Noda, G. Imataka, and H. Kurahashi. 2009. Outcome of acute
736 necrotizing encephalopathy in relation to treatment with corticosteroids and
737 gammaglobulin. *Brain Dev.* 31:221–227. doi:10.1016/j.braindev.2008.03.005.

738 Portilho, D.M., J. Fernandez, M. Ringeard, A.K. Machado, A. Boulay, M. Mayer, M. Müller-
739 Trutwin, A.-S. Beignon, F. Kirchhoff, S. Nisole, and N.J. Arhel. 2016. Endogenous TRIM5α
740 Function Is Regulated by SUMOylation and Nuclear Sequestration for Efficient Innate
741 Sensing in Dendritic Cells. *Cell Rep.* 14:355–369. doi:10.1016/j.celrep.2015.12.039.

742 Sakuma, H., T. Thomas, C. Debinski, M. Eyre, V.X. Han, H.F. Jones, G. Kawano, V.W. Lee, S.
743 Malone, T. Matsuishi, S.S. Mohammad, T. Mori, H. Nishida, M. Nosadini, J.-I. Takanashi,
744 M. Mizuguchi, M. Lim, and R.C. Dale. 2025. International consensus definitions for
745 infection-triggered encephalopathy syndromes. *Dev. Med. Child Neurol.* 67:195–207.
746 doi:10.1111/dmcn.16067.

747 Schaller, T., K.E. Ocwieja, J. Rasaiyaah, A.J. Price, T.L. Brady, S.L. Roth, S. Hué, A.J. Fletcher, K.
748 Lee, V.N. KewalRamani, M. Noursadeghi, R.G. Jenner, L.C. James, F.D. Bushman, and G.J.
749 Towers. 2011. HIV-1 Capsid-Cyclophilin Interactions Determine Nuclear Import Pathway,
750 Integration Targeting and Replication Efficiency. *PLOS Pathog.* 7:e1002439.
751 doi:10.1371/journal.ppat.1002439.

752 Shen, Q., Y.E. Wang, M. Truong, K. Mahadevan, J.J. Wu, H. Zhang, J. Li, H.W. Smith, C.A. Smibert,
753 and A.F. Palazzo. 2021. RanBP2/Nup358 enhances miRNA activity by sumoylating
754 Argonautes. *PLOS Genet.* 17:e1009378. doi:10.1371/journal.pgen.1009378.

755 Sugaya, N. 2002. Influenza-associated encephalopathy in Japan. *Semin. Pediatr. Infect. Dis.*
756 13:79–84. doi:10.1053/spid.2002.122993.

757 Watanabe, K., N. Takizawa, M. Katoh, K. Hoshida, N. Kobayashi, and K. Nagata. 2001. Inhibition
758 of nuclear export of ribonucleoprotein complexes of influenza virus by leptomycin B.
759 *Virus Res.* 77:31–42. doi:10.1016/S0168-1702(01)00263-5.

760 Watanabe, T., S. Watanabe, and Y. Kawaoka. 2010. Cellular Networks Involved in the Influenza
761 Virus Life Cycle. *Cell Host Microbe*. 7:427–439. doi:10.1016/j.chom.2010.05.008.

762 Wu, J., M.J. Matunis, D. Kraemer, G. Blobel, and E. Coutavas. 1995. Nup358, a Cytoplasmically
763 Exposed Nucleoporin with Peptide Repeats, Ran-GTP Binding Sites, Zinc Fingers, a
764 Cyclophilin A Homologous Domain, and a Leucine-rich Region. *J. Biol. Chem.* 270:14209–
765 14213. doi:10.1074/jbc.270.23.14209.

766 Wu, X., W. Wu, W. Pan, L. Wu, K. Liu, and H.-L. Zhang. 2015. Acute Necrotizing Encephalopathy:
767 An Underrecognized Clinicoradiologic Disorder. *Mediators Inflamm.* 2015:792578.
768 doi:10.1155/2015/792578.

769 Yokoyama, N., N. Hayashi, T. Seki, N. Panté, T. Ohba, K. Nishii, K. Kuma, T. Hayashida, T. Miyata,
770 U. Aebi, M. Fukui, and T. Nishimoto. 1995. A giant nucleopore protein that binds
771 Ran/TC4. *Nature*. 376:184–188. doi:10.1038/376184a0.

772 Zhang, R., R. Mehla, and A. Chauhan. 2010. Perturbation of Host Nuclear Membrane
773 Component RanBP2 Impairs the Nuclear Import of Human Immunodeficiency Virus -1
774 Preintegration Complex (DNA). *PLoS ONE*. 5:e15620. doi:10.1371/journal.pone.0015620.

775 Zhu, Z., E. Fodor, and J.R. Keown. 2023. A structural understanding of influenza virus genome
776 replication. *Trends Microbiol.* 31:308–319. doi:10.1016/j.tim.2022.09.015.

777